AN ABSTRACT OF THE THESIS OF

MULPURI VENKATA RAO for the degree of Doctor of Philosophy in Electrical and Computer Engineering presented on January 11, 1985.

Title: Properties of Semi-Insulating $In_{0.53}Ga_{0.47}As$ Epitaxial Layers and Photoconductive Detectors

Redacted for privacy

Abstract approved: ______________________
Dr. P. K. Bhattacharya

The growth of very high purity undoped and Fe-, Cr- and Zn-doped $In_{0.53}Ga_{0.47}As$ by liquid phase epitaxy using extended melt-baking schemes has been investigated. The epitaxial layers were characterized by Hall and photoluminescence measurements. High purity undoped layers having N_D and $N_A \leq 5 \times 10^{14}$ cm^{-3} and with μ_{300K} and μ_{77K} = 10,200 and 60,000 $cm^2/V.s$, respectively, could be reproducibly grown by 20 -40 hr baking of the melt In followed by 20 - 40 hr baking of In + InAs + GaAs in an ultrapure H_2 ambient. These material parameters are amongst the best values obtained for this ternary alloy. The most intense peaks in the edge photoluminescence at 4.4K arise from a family of bound excitons. Impurity-related transitions observed in the spectra were associated with Zn acceptors having E_A = 28.0 ±

1.0 meV and C acceptors having E_A = 13.0 $\pm$ 1.0 meV. A deep level at 0.18 eV below the conduction band was detected in heat-treated high-purity $In_{0.53}Ga_{0.47}As$ layers. Fe-doped layers with (N_D-N_A) as low as 2.0×10^{12} cm^{-3} and $\mu_n \sim 6000$ $cm^2/V.s$ were grown consistently for the first time. An ionization energy of 0.46 eV for Fe acceptors is found from the analysis of temperature-dependent Hall data, with no additional feature in the 4.2K band-edge photoluminescence spectra. Cr doping seems to produce a donor-like center with an apparent ionization energy of 24 meV. It is believed that Cr itself, or a complex defect involving Cr, is responsible for the formation of the donor-like center. p-type material with $(N_A - N_D)$ as low as 2×10^{15} cm^{-3} has been grown by a novel doping technique using Zn.

Planar interdigitated and source-drain photoconductive detectors were fabricated on high-resistivity liquid phase epitaxial $In_{0.53}Ga_{0.47}As/InP$ doped with Fe for the first time. Dark currents in these devices are in the μA range. A dark noise power of -108.9 dBm is observed at 82°C. The devices show good spectral response in the range 1.3 - 1.7 μm and a response time of about 100ps for 300ps excitation pulses. The optical gains measured in the devices are $\sim$ 6-10 and are amongst the highest values reported for similar devices. The performance characteristics have been measured and analyzed and have been compared with identical devices made from Zn-doped $In_{0.53}Ga_{0.47}As$.

PROPERTIES OF SEMI-INSULATING $In_{0.53}Ga_{0.47}As$ EPITAXIAL LAYERS AND PHOTOCONDUCTIVE DETECTORS

By

Mulpuri Venkata Rao

A THESIS

submitted to

Oregon State University

in partial fulfillment of
the requirements for the
degree of
Doctor of Philosophy

Completed January 11, 1985

Commencement June 1985

APPROVED:

Redacted for privacy

Associate Professor of Electrical and Computer Engineering
in charge of major

Redacted for privacy

Head of Department of Electrical and Computer Engineering

Redacted for privacy

Dean of Graduate School

Date Thesis is Presented: January 11, 1985

Typed by Cynthia Kinsey for Mulpuri Venkata Rao

ACKNOWLEDGEMENTS

I wish to express my deep gratitude to my advisor Professor P. K. Bhattacharya, for his guidance and encouragement during the course of this work. I would like to express my sincere appreciation to Dr. C. Y. Chen of AT&T Bell Laboratories, Murray Hill, for his help in performing some device measurements. I am indebted to my senior Dr. J. K. Rhee for teaching me how to grow the LPE material. The support provided by National Science Foundation and University of Michigan where part of this work was performed is gratefully acknowledged. I wish to thank Professor W. J. Fredericks (Department of Chemistry) for allowing me to use some facilities in his laboratory and, J. Swenson (University of Michigan) and L. Shive (University of Michigan) for their technical assistance.

Finally, I would like to thank my parents for their encouragement during my entire studies and my wife, Savitri, for her patience and support.

TABLE OF CONTENTS

	Page
I. INTRODUCTION	1
II. LIQUID PHASE EPITAXIAL (LPE) GROWTH OF $In_{0.53}Ga_{0.47}As$	6
2.1 Growth System	6
2.2 Materials Preparation for Epitaxial Growth	8
2.3 LPE Growth Process	8
2.4 Growth of Fe-, Cr- and Zn-Doped Epitaxial Layers	11
2.5 Discussion	12
III. PROPERTIES OF UNDOPED AND DOPED $In_{0.53}Ga_{0.47}As$	16
3.1 Characteristics of High-Purity $In_{0.53}Ga_{0.47}As$	16
3.1.1 Hall Measurements and Analysis of Data	16
3.1.2 Photoluminescence (PL) Measurements	20
3.1.3 PL Spectra Results and Discussion	20
3.2 Postgrowth Heat-Treatment Effects in High-Purity LPE $In_{0.53}Ga_{0.47}As$	26
3.3 Characterization of Fe- and Cr-Doped $In_{0.53}Ga_{0.47}As$	29
3.3.1 Electrical Properties	29
3.3.2 Photoluminescence Measurements on High-Resistivity $In_{0.53}Ga_{0.47}As$	39
3.3.3 Discussion	39
3.4 Properties of Zn-Doped $In_{0.53}Ga_{0.47}As$	43
3.4.1 Electrical Characteristics	43
3.4.2 Photoluminescence Data	46
3.4.3 Discussion	49

IV. THEORY OF PHOTOCONDUCTIVE DETECTORS 50

4.1 Types of Photoconduction 50

4.2 Mechanism of Intrinsic Photoconduction 53

4.3 Photoconductive Gain 55

4.4 Material Considerations for Photoconductive Detectors 57

V. PERFORMANCE CHARACTERISTICS OF $In_{0.53}Ga_{0.47}As$ PHOTOCONDUCTIVE DETECTORS 59

5.1 Device Fabrication 59

5.2 Dark Current-Voltage Characteristics 59

5.3 Device Results and Discussion 61

5.3.1 Spectral Response 61

5.3.2 Impulse Response of $In_{0.53}Ga_{0.47}As$:Fe Photodetector 64

5.3.3 D.C. Optical Gain Measurements 69

5.3.4 Noise Characteristics 74

VI. CONCLUSIONS 81

REFERENCES 84

APPENDICES

Appendix I 90

Appendix II 94

Appendix III 96

Appendix IV 99

LIST OF FIGURES

Figure		Page
2.1	Schematic diagram of the liquid phase epitaxy system.	7
2.2	Time-temperature cycle for a typical epitaxial growth run.	10
2.3	Photomicrographs showing the surface morphology of (a) undoped and (b) Fe-doped (X^{l}_{Fe} = 3.0 x 10^{-4}) $In_{0.53}Ga_{0.47}As/InP$ grown by liquid phase epitaxy.	13
3.1	Temperature dependence of the Hall electron mobility in LPE $In_{0.53}Ga_{0.47}As$ layers of varying purity. The solid lines indicate the theoretically calculated mobilities.	19
3.2	Edge photoluminescence observed at 4.4 K for four crystals in increasing order of purity.	21
3.3	Variation in the character of the main peak with temperature in the edge luminescence of sample OS-7.	23
3.4	Variation of Hall mobility in as-grown and heat treated samples of LPE $In_{0.53}Ga_{0.47}As$ grown after extended baking of In melt alone.	27
3.5	Photoluminescence spectra of as-grown and heat-treated $In_{0.53}Ga_{0.47}As$.	28

Figure

Page

3.6 Variation of Hall electron concentration in LPE $In_{0.53}Ga_{0.47}As$ (a) before and (b) after heat treatment. 30

3.7 Variation of Hall electron concentration at room temperature with X^{l}_{Fe} in LPE $In_{0.53}Ga_{0.47}As$. 31

3.8 Variation of Hall electron concentration with inverse temperature in Fe-doped LPE $In_{0.53}Ga_{0.47}As$. 34

3.9 Temperature dependence of Hall electron mobility in Cr-doped LPE $In_{0.53}Ga_{0.47}As$. 37

3.10 Variation of Hall electron concentration with inverse temperature in Cr-doped LPE $In_{0.53}Ga_{0.47}As$. 38

3.11 Edge photoluminescence observed at 4.2 K for (a) undoped, (b) Fe-doped, and (c) Cr-doped LPE $In_{0.53}Ga_{0.47}As$. 40

3.12 Variation of Hall hole concentration at room temperature with X^{l}_{Zn} in LPE $In_{0.53}Ga_{0.47}As$. 44

3.13 Temperature dependence of Hall hole mobility in Zn-doped LPE $In_{0.53}Ga_{0.47}As$. 47

3.14 Edge photoluminescence spectra of Zn-doped LPE $In_{0.53}Ga_{0.47}As$ at 4.2 K. 48

4.1 Photoconduction transitions (a) intrinsic, (b) extrinsic involving donor levels and (c) extrinsic involving acceptor levels. 51

Figure		Page
4.2	Cross-sectional view of a lateral photoconductive detector.	54
5.1	(a) SEM photomicrograph of $In_{0.53}Ga_{0.47}As:Fe$ photoconductive detector, (b) dark current-voltage characteristics for a planar source-drain photoconductive detector.	60
5.2	Schematic for spectral response measurements.	62
5.3	Spectral response of $In_{0.53}Ga_{0.47}As:Fe$ photoconductive detector measured at a bias of 2V.	63
5.4	Photoresponse of $In_{0.53}Ga_{0.47}As:Fe$ photoconductive detector at 6V bias to (a) 300 ps and (b) 11 ns pulses provided by 1.29µm InGaAsP laser.	65
5.5	Variation of peak photovoltage with bias in $In_{0.53}Ga_{0.47}As:Fe$ photoconductive detector	68
5.6	Setup for dc optical gain measurements.	70
5.7	Variation of internal optical gain with bias in $In_{0.53}Ga_{0.47}As:Fe$ and $In_{0.53}Ga_{0.47}As:Zn$ photoconductors.	71
5.8	Variation of internal optical gain with temperature at various levels of excitation intensity.	73

Figure		Page
5.9	Variation of internal optical gain with applied bias at various levels of excitation intensity.	75
5.10	Schematic for noise measurements	77
5.11	Variation of dark current with temperature in $In_{0.53}Ga_{0.47}As$:Fe photoconductive detector.	78
5.12	Dependence of noise power on frequencies in $In_{0.53}Ga_{0.47}As$:Fe photoconductive detector.	79

LIST OF TABLES

Table		Page
3.1	Electrical properties of undoped LPE $In_{0.53}Ga_{0.47}As$.	17
3.2	Electrical properties of Fe-doped LPE $In_{0.53}Ga_{0.47}As$.	32
3.3	Electrical properties of Cr-doped LPE $In_{0.53}Ga_{0.47}As$.	36

LIST OF SYMBOLS

A	Atomic weight
c	Velocity of light (3×10^8 m/sec)
C_l, C_s	Concentration of the impurity in liquid and solid phase (cm^3)
E_A, E_D	Shallow acceptor and donor ionization energy (eV)
E_{AA}	Deep acceptor ionization energy (eV)
E_F	Fermi-energy in semiconductor (eV)
E_G	Forbidden energy gap of a semiconductor (eV)
G_{opt}	Optical gain of photoconductive detector
g_{AA}	Degeneracy factor for deep acceptors
h	Plank's constant (6.62×10^{-34} J.sec)
k	Boltzmann's constant (1.38×10^{-23} J/K)
K_s	Segregation coefficient for impurity.
K	Equilibrium constant for the chemical reaction.
L	Active channel length of photoconductive detector
m_e^*	Electron effective mass
m_{hh}^*, m_{lh}^*	Heavy and light hole effective mass
m_o	Free electron mass (9.1×10^{-31} kg)
N_A, N_D	Shallow acceptor and donor concentration (cm^{-3})
N_{AA}	Concentration of deep acceptor (cm^{-3})
N_c	Effective density of states in the conduction band (cm^{-3})
N_L	Avagadro's number (6.02×10^{23})
n, p	Free electron and hole concentrations in semiconductors (cm^{-3})

n_i	Intrinsic carrier concentration (cm^{-3})
Δn	Excess concentration of electrons (cm^{-3})
Q	Electron-hole pair generation rate ($cm^{-3}.sec^{-1}$)
q	Electron charge (1.6×10^{-19} coulombs)
R	Reflection coefficient
t_r	Carrier transit time (sec)
W	Incident light power (Watts)
χ_i^l	Atomic fraction of element i in the liquid
α	Absorption coefficient
$h\nu$	Photon energy (eV)
ε_o	Absolute permitivity of free space (8.85×10^{-4} F/cm)
ε_s	Static dielectric constant
τ_n, τ_p	Excess electron and hole lifetimes (sec)
μ_H	Hall mobility ($cm^2/V.s$)
μ_n, μ_p	Mobility of electrons, holes ($cm^2/V.s$)
ρ	Material density (g/cm^3)
λ	Wavelength (nm)
η_i	Internal quantum efficiency
Γ	Photoconductive gain

PROPERTIES OF SEMI-INSULATING $In_{0.53}Ga_{0.4}As$ EPITAXIAL LAYERS AND PHOTOCONDUCTIVE DETECTORS

CHAPTER I

INTRODUCTION

$In_{0.53}Ga_{0.47}As$ lattice-matched to InP has emerged as a semiconductor which is important for present-day opto-electronic and microwave device applications[1,2]. In view of the high electron mobilities and drift velocities calculated[3] and measured[4] in this alloy it is an attractive material for fabricating high speed field-effect transistors using ion-implantation or suitable alternate technology. The mobility in this compound is considerably higher than those in GaAs and InP. The room-temperature bandgap of 0.74 eV in $In_{0.53}Ga_{0.47}As$ makes it useful as a photodetector material in fiber-optical communication systems operating at wavelengths between 1.1 and 1.7μm. Undoped and doped n- and p-type $In_{0.53}Ga_{0.47}As$ have been grown on InP by liquid phase epitaxy (LPE) for the above applications[1,5-8]. It is necessary, for some of these applications, to have epitaxial material of near-intrinisic nature exhibiting high resistivity and p-type material with $(N_A-N_D) \sim 10^{15}$ cm^{-3}. At the same time, to maintain high carrier mobilities and reproducible carrier densities the residual impurity concentrations must be sufficiently low before adding the appropriate dopant into the growth

melt. Therefore, the first stage of this work was aimed at achieving high purity LPE layers with low residual doping.

It is known that extended baking of LPE growth solutions in a pure H_2 ambient improves the purity of the epitaxial layer[4,9]. It has also been reported that trace amounts of H_2O[4,10,11] or O_2[12,13] added to the H_2 ambient reduce the impurity in the growth solutions even further, thereby enhancing the purity of the layer. Controlled amounts of moisture added to the growth ambient have resulted in epitaxial layers of extremely high purity[9], but the danger of the lack of proper control always exists. Extended baking of the In melt and source InAs and GaAs forming the growth solution is known to lower the levels of both donor (Si and S)[4] and acceptor (Al, Mg, Zn)[9] impurities in the grown epitaxial layer.

In this study, different melt-baking schemes in ultrapure H_2 ambient, without the intentional introduction of moisture, have been used to obtain high-purity layers. Initially the effects of extended In baking alone on the purity of the grown layers were studied. Subsequently, the effects of baking the In followed by baking of In + InAs + GaAs were examined. Layers with low free-electron concentration ($n \sim 10^{14} - 10^{15}$ cm^{-3}) and high electron mobility were obtained. Slightly lower values of n were obtained by compensating the residual shallow donors with controlled addition of Zn, which gives rise to shallow acceptors. In order to reduce the free-electron concentration even further, an

attractive method is to introduce deep levels in the energy bandgap of the material. This technique has been successfully employed to grow high-resistivity GaAs by LPE[14-18] and is widely used to grow semi-insulating bulk crystals of GaAs and InP. Since Cr and Fe are generally used as the dopant species to produce compensating deep levels in GaAs and InP, the doping of LPE $In_{0.53}Ga_{0.47}As$ with these elements has been investigated.

Some of the underlying problems should be highlighted. The ternary semiconductor has a bandgap of 0.74 eV at room temperature and $n_i(300K) = 5.5 \times 10^{11}$ cm^{-3} assuming m_e^*/m_o and m_h^*/m_o = 0.034 and 0.45, respectively[19,20]. Therefore the maximum attainable resistivity in this semiconductor will not be as high as that in GaAs or InP (> 10^7 ohm-cm). As reported earlier[14-18], the growth of semi-insulating LPE GaAs requires close compensation of shallow donors and acceptors arising from residual impurities in the source materials and from chemical reactions between the growth system components. Further enhancement of the resistivity is obtained by the addition of Cr which forms a deep acceptor level in GaAs. However, this cannot always be achieved[14]. In addition, attempts to grow high-resistivity LPE InP by Fe, Cr and Co doping have been unsuccessful[21].

Clawson et al.[22] have recently reported resistivity and mobility data of Fe-doped LPE $In_{0.53}Ga_{0.47}As$. There is no report on Cr-doping of LPE $In_{0.53}Ga_{0.47}As$. In this study, the doping of the ternary alloy with Fe and Cr has been investigated in detail.

Furthermore, the growth of lightly doped p-$In_{0.53}Ga_{0.47}As$ for the fabrication of photoconductive detectors has been investigated using a novel Zn-doping technique.

Undoped and doped epitaxial layers were characterized by variable-temperature Hall and high-resolution photoluminescence (PL) measurements. PL measurements on $In_{0.53}Ga_{0.47}As$ grown by LPE, vapor phase epitaxy (VPE), and molecular beam epitaxy (MBE) have been reported[1,23-28] but a definite identification of the peaks contained in the edge luminescence of high-quality materials was lacking. From Hall data the distribution coefficients of Fe and Zn and the energy position of the deep level produced by Fe have been determined. In the case of Cr-doping, use of a melt-baking scheme identical to that for Fe-doping failed to produce high-resistivity $In_{0.53}Ga_{0.47}As$. Hall and low-temperature PL measurements indicate that a shallow level, which presumably acts as a donor, is produced by the incorporation of Cr and increases the conductivity.

Photoconductive detectors have advantages over photodiodes because of simplicity of fabrication, uniformity, and their potential for achieving photoconductive gains greater than unity. The gain of a photoconductive detector (defined as the number of carriers collected in the external circuit per incident photon) is approximately given by the ratio τ/t_r where t_r and τ are the carrier transit time and lifetime, respectively. Devices with a short electrode spacing have large gains, short response times

and large gain bandwidth products. Carrier recombination and transit times in these devices are independent, so that speed, gain, and device dimensions can be traded off against each other depending on the desired application. The performance of photoconductive detectors made on n- and p-type $In_{0.53}Ga_{0.47}As$ and modulation doped $In_{0.53}Ga_{0.47}As/In_{0.52}Al_{0.48}As$ heterostructures has been reported.[29-36] However, the performance of detectors made with the high resistivity ternary compound has not been demonstrated. A useful application is the integration of such detectors with FETs made with the same high-resistivity material[37] to form the front end of an optical receiver. It is therefore essential that the carrier mobilities in the high-resistivity material be as high as possible.

In this work, the spectral response; bias, temperature- and incident light intensity-dependent gain, optical pulse response and noise characteristics of photoconductive detectors made on Fe-doped SI $In_{0.53}Ga_{0.47}As$ have been studied. Comparisons of the optical gains have been made with identical devices made on Zn-doped p-type $In_{0.53}Ga_{0.47}As$. It is observed that the devices made on high resistivity $In_{0.53}Ga_{0.47}As$ have the lowest noise, highest speed and optical gains comparable with identical devices made on p-type $In_{0.53}Ga_{0.47}As$.

CHAPTER II

LIQUID PHASE EPITAXIAL (LPE) GROWTH OF $In_{0.53}Ga_{0.47}As$

2.1 Growth System

The schematic of the liquid phase epitaxial (LPE) growth system is shown in Fig. 2.1(a). The semitransparent furnace tube, gold-coated on the inside, has a constant temperature profile within 1°C over 50% of the length of the heating coil. the furnace temperature is controlled by a EUROTHERM Model 931 SCR power supply, and a EUROTHERM Model 917 controller with the aid of a chromel-alumel thermocouple. The reaction tube is made of suprasil quartz. The temperature of the growth cell is monitored by a chromel-alumel thermocouple placed inside the graphite boat. The temperature variation during epitaxial growth is achieved by a EUROTHERM Model 125 programmer. The graphite boat was first heated at 1000°C for 4 hr under a vacuum of 2×10^{-7} torr and then back-filled with He. The boat was then loaded in the reaction tube and all the grooves were filled with 99.9999% pure In (Johnson Matthey) and baked at 730°C for about 100 hr under Pd-diffused H_2 flow. This purging step is crucial for the removal of residual impurities in the walls of the boat.

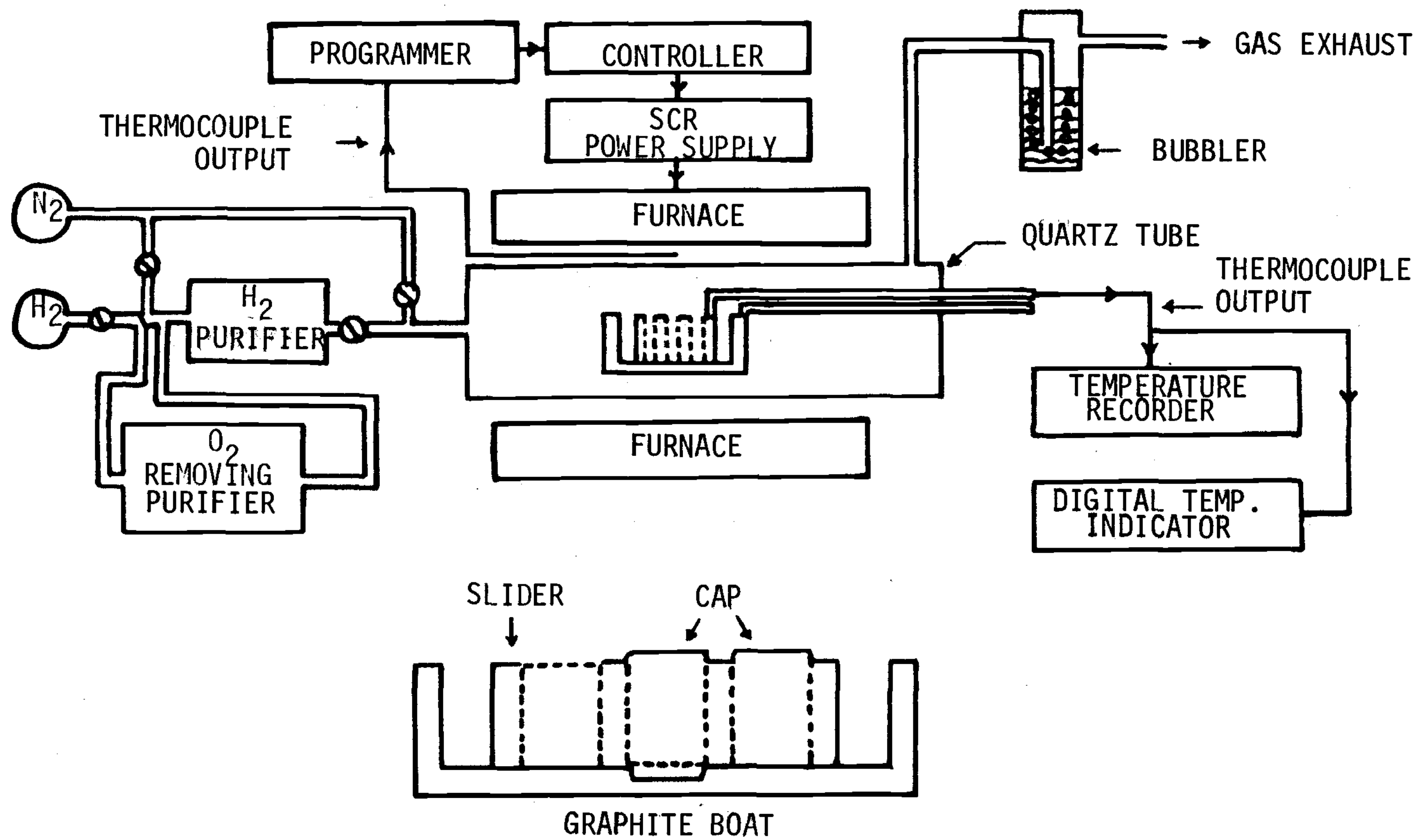

Figure 2.1 Schematic diagram of the liquid phase epitaxy system.

2.2 Materials Preparation for Epitaxial Growth

The etch-pit density in the (100)-oriented InP:Fe substrates grown by the liquid encapsulation Czochralski (LEC) technique, was less than 5×10^3 cm^{-2}. The surface morphology of the polished substrates was further improved by chemi-mechanical polishing on KODAK lens-cleaning paper in successively weaker bromine methanol solutions. The polished substrate was degreased by boiling sequentially in electronic grade trichloroethylene (TCE), acetone, and isopropyl alcohol (IPA). The substrate was then etched for 30 sec in (2:1) H_2O:HCl and vigorously rinsed in de-ionized water (18 MΩ) followed by a rinse in IPA. The substrate was finally dried in IPA vapor before loading onto the boat. The same procedure was used to clean the source materials: polycrystalline InAs, polycrystalline GaAs and high-purity In. Indium and InAs were etched in (2:1) H_2O:HNO_3, whereas GaAs was etched in (1:1) H_2O:HCl for 1-2 min.

2.3 The LPE Growth Process

The solution composition used for the growth of lattice-matched $In_{0.53}Ga_{0.47}As$ on (100)-oriented InP:Fe substrates were derived from phase equilibrium calculation of the In-Ga-As system[38]. The atomic fractions of the elements constituting the melt for growth at 650°C are $X^l_{Ga} = 0.0259$, $X^l_{In} = 0.9123$ and $X^l_{As} = 0.0618$. The time-temperature cycle for a typical

epitaxial growth run is depicted in Fig. 2.2. The horizontal graphite boat was first loaded with 4g In for the in-situ melt etch and 2.68482g In for the growth melt, which were then baked at 730°C for periods ranging from 20-100 hr (A to B) in the Pd-diffused H_2 ambient. Before each baking step, the reaction tube was sealed and purged with purified H_2 for at least one and a half hours. The system was cooled and appropriate amounts of polycrystalline GaAs and InAs were added to the growth melt at time C to form the growth solution. A suitable amount of polycrystalline InP was added to the In for in-situ etching to obtain a slightly undersaturated melt at the growth temperatures. After purging with H_2 for one and a half hours (C to D), the In-Ga-As growth solution and etch melt were baked initially at 730°C and subsequently at lower temperatures up to 680°C, with the total baking time being varied for each run (E to F). During this period, the in-situ etch melt was covered with a graphite cap to prevent evaporation of P atoms. At time G, the polished and cleaned substrate was loaded into the boat at room temperature. The growth system was again purged with H_2 for one and a half hours (G to H). The temperature was then raised to and held at 651°C for 30 minutes for the melt homogenization (I to J). During this period, the substrate was covered with a graphite cap to minimize surface evaporation of P atoms. A cooling ramp was then set in the programmer-controller and the boat with its contents were cooled at 0.1°C/min. When the temperature of

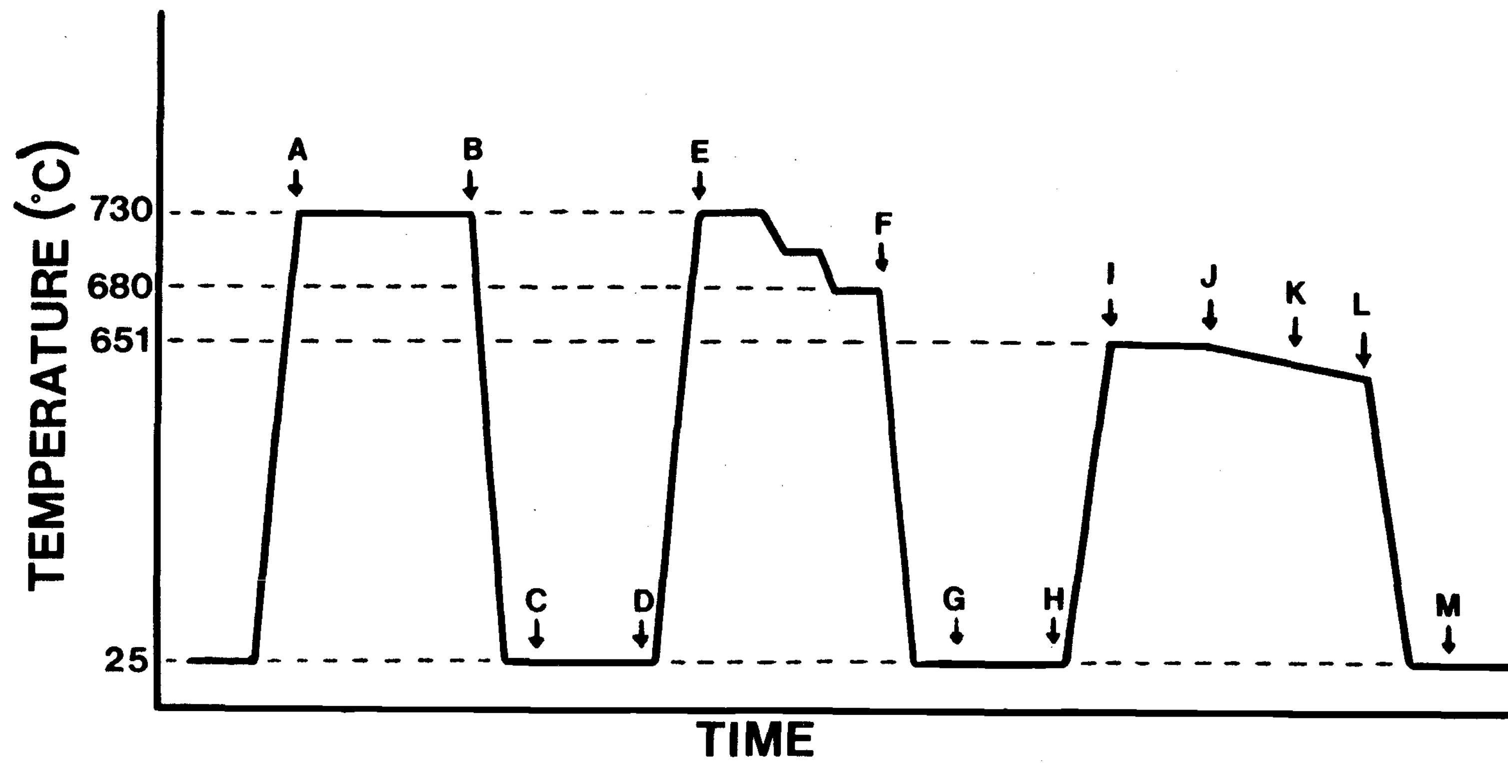

Figure 2.2 Time-temperature cycle for a typical epitaxial growth run.

the growth melt reached 647°C (time K), in-situ etching of the substrate was accomplished by sliding the undersaturated In melt on top of the substrate for 3-5 seconds. Epitaxial growth was then initiated by pulling the In-Ga-As saturated melt solution on the substrate. Growth was terminated after 10 minutes (time L) by sliding the melt away from the grown epitaxial layer. The furnace was then cooled to room temperature, and the epitaxial layer was removed from the boat (time M) and any melt remaining on its surface was removed by dipping in Hg at room temperature. A particular melt was used for two or three consecutive growth runs with a reduction of the growth temperature by approximately 2°C for each successive run.

2.4 Growth of Fe-, Cr- and Zn-Doped Epitaxial Layers

The melt composition used for the growth of doped epitaxial layers was the same as that of undoped layers. Typically a melt baking scheme was employed such that the residual donor and acceptor impurity concentrations in the epitaxial layers were no more than 5×10^{15} cm^{-3}. Controlled amounts of Fe or Cr were added at the time of substrate loading after the melt baking. this was done to avoid oxidation reactions taking place in the quartz reaction tube. The upper limit on $X^{l}_{Fe/Cr}$ in this work was determined by melt carry-over problems and/or degradation in surface morphology. The surface morphology of a typical undoped sample and a Fe-doped sample (X^{l}_{Fe} = 3.0×10^{-4}) is shown in

the photomicrographs of Fig. 2.3(a) and (b), respectively for comparison.

Since the distribution coefficient of Zn in III-V semiconductors is very large, hole concentrations in Zn-doped $In_{0.53}Ga_{0.47}As$ in the range of 10^{15} to 5×10^{16} cm^{-3} was accomplished by using Zn-doped GaAs ($N_A - N_D = 1 \times 10^{18}$ cm^{-3}) as the dopant source. The required amount of GaAs:Zn was added to the melt at the time of substrate loading. This was done to avoid Zn evaporation during melt baking due to its high vapor pressure.

2.5 Discussion

Si and S have been identified as the most dominant donor impurities in $In_{0.53}Ga_{0.47}As$[39]. Minute traces of O_2 and H_2O present in the ambient H_2, and O_2 and H_2O present in In are sufficient for the removal of residual Si in the melt constituents by its conversion to SiO_2 according to the net reaction:

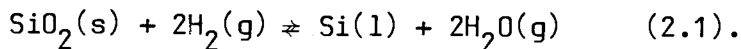

$$SiO_2(s) + 2H_2(g) \rightleftharpoons Si(l) + 2H_2O(g) \qquad (2.1).$$

The compound SiO_2 is usually not incorporated in the epitaxial layer. In addition, an increasing dissociation of SiO_2 from the quartz tube with increasing temperature according to Eqn. 2.1 is also assumed to serve as a source of H_2O in the ppm range[4,9]. The equilibrium concentration of Si in the solution is given by:

$$[Si]_l = K(T)/[H_2O]_g^2 \qquad (2.2)$$

where K(T) is the equilibrium constant for the reaction expressed in Eqn. 2.1. Extended baking of the In melt and In-Ga-As growth

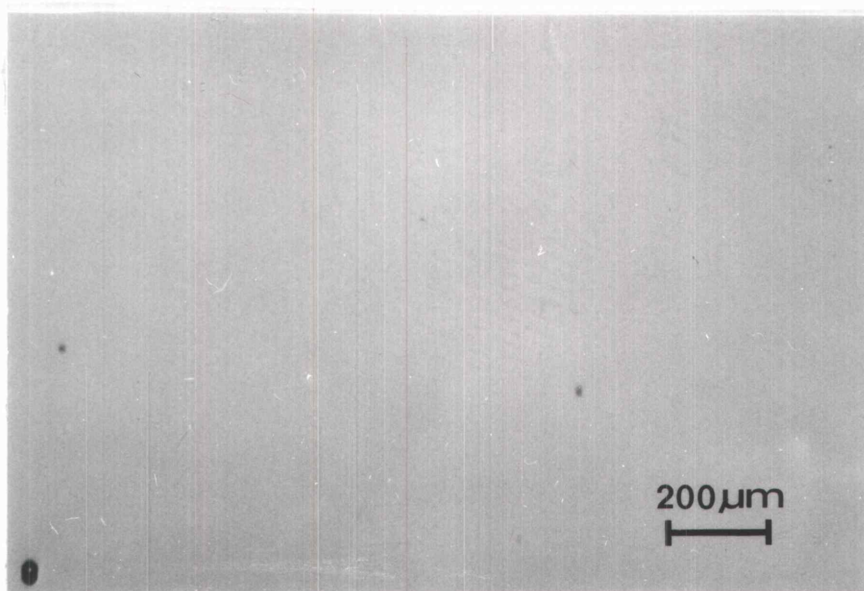

(a)

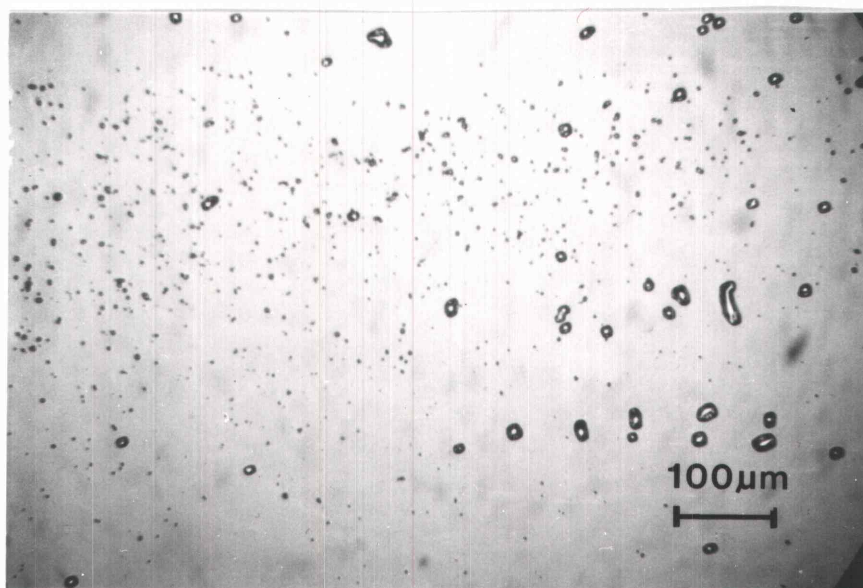

(b)

Figure 2.3 Photomicrographs showing the surface morphology of (a) undoped and (b) Fe-doped (X^{l}_{Fe} = 3.0 x 10^{-4}) $In_{0.53}Ga_{0.47}As/InP$ grown by liquid phase epitaxy.

solution is known to lower the levels of both donor (Si and S)[4] and acceptor (Al, Mg, Zn)[9] impurities in the grown epitaxial layer. As mentioned earlier, the melt was initially baked at 730°C and subsequentially at lower temperatures up to 680°C. A high baking temperature is effective in reducing the concentration of volatile impurities such as S. However, the equilibrium concentration of Si and certain acceptor impurities is found to be less in crystals grown from melts baked at lower temperatures[13]. The amount of As evaporation during melt baking at temperatures around 700°C is nearly zero since $X^{l}_{As} = 0.0618$ is very small[39]. The influence of As evaporation on the lattice mismatch a/a of the layers can be almost ignored for baking temperatures around 700°C[39].

In this study (100)-oriented InP was used as substrates in preference to (111) B oriented crystals due to the following reasons. The growth rate of the alloy is almost twice as high on the (100) face compared to that on the (111) B face[40]. The growth rate differences may be caused by different nucleation densities for the two orientations[41]. The segregation coefficient $K_s (= C_s/C_l)$ of impurities and vacancies is approximately one order of magnitude larger on the (111) B face than it is on the (100) face[42]. It is important to mention that different solution compositions are required to grow lattice-matched layers on (100) and (111) B substrates. This is due to a larger

distribution coefficient of Ga on the (100) face than on the (111) B face and vice-versa for As[41].

Heating of InP at temperatures higher than the congruent evaporation temperature of 370°C causes preferential evaporation of P atoms and degrades the surface morphology. High-quality layers cannot therefore be grown directly on InP substrates thermally damaged during melt equilibration at 651°C. The use of a graphite cover for the substrate during heating and melt homogenization and in situ etching before initiation of growth are indispensable in LPE growth on InP substrate. In this study, controllability over in-situ etch removal was achieved by varying the degree of in-situ melt undersaturation with P and the etching period. The melt-back should be shallow because In is a crystallographically preferential etchant. Furthermore, deep melt-backs are known to give rise to melt carryover problems[43].

Epitaxial layer thicknesses were estimated by delineating the epitaxial layer-substrate junction on a cleaved face by the AB dislocation etch technique[44]. The thickness of the epitaxial layer was accurately measured by a calibrated microscope. Typical layer thickness varied from 6 to 8 μm for 10 minutes growth.

CHAPTER III

PROPERTIES OF UNDOPED AND DOPED $In_{0.53}Ga_{0.47}As$

Measurements performed on undoped and Fe-, Cr- and Zn-doped $In_{0.53}Ga_{0.47}As$ and the results therefrom are presented in this chapter. Measurements on heat-treated undoped $In_{0.53}Ga_{0.47}As$ are also included. The experimental data are analyzed and discussed.

3.1 Characterization of High-Purity $In_{0.53}Ga_{0.47}As$

3.1.1 Hall Measurements and Analysis of Data

The free carrier concentration and Hall electron mobility in the epitaxial layers were measured in the temperature range of 10-300K by the van der Pauw technique. Contacts to the samples were provided by alloying In-Sn. Measurements were performed with the lowest possible currents and a magnetic field of 0.4 Tesla. A unity Hall factor has been assumed.

A representative set of the measured electrical characteristics is listed in Table 3.1. A marked improvement in mobility was achieved by baking In alone for 20 hrs. Thereafter, no significant improvement in mobilities were observed even for In baking durations of up to 100 hrs. Significant improvement in mobility values was achieved by baking the entire growth solution subsequent to baking the In alone. Here also, the best results

Table 3.1 Electrical Properties of Undoped LPE $In_{0.53}Ga_{0.47}As$

Samples	Melt baking scheme	Measured N_D-N_A ($\times 10^{15}$) at 300K (cm^{-3})	Measured μ_H at 300K ($cm^2/V.s$)	Measured highest low-temperature mobility ($cm^2/V.s$)
OS-0	no baking	27.0	4400	6,700
OS-1	20-h In	2.0	6320	19,000
OS-2	60-h In	2.4	6150	18,700
OS-3	80-h In	1.9	6950	18,500
OS-4	100-h In	2.2	6910	18,150
OS-5	40-h In + 2.5-h melt	2.1	8070	29,800
OS-6	0-h In + 10-h melt	1.0	6530	33,400
OS-7	20-h In + 20-h melt	0.06	9000	54,100
OS-8	20-h In + 60-h melt	0.25	6900	55,000

were obtained by 20 hrs baking of the In followed by 20-60 hrs baking of the entire melt. The highest mobility values obtained in this study were μ_{300K} = 10,200 $cm^2/V.s$ and μ_{77K} = 55-60,000 $cm^2/V.s$. The improvement observed due to baking of In followed by baking of the entire growth solution is in agreement with the observations of Cook et al.(45) and Kuphal and Pocker(9). The highest mobilities in this study, both at 300 and 77 K, compare very favorably with the data of these authors. Higher mobilities in this alloy have been obtained for LPE growth on (111) B InP substrates(4). Extended baking is beneficial up to the point where the removal of impurities is balanced by incorporation of C from the boat and other impurities in the growth system. This explains the minimal gain beyond an In or melt baking of 20 hrs each. The results also indicate that reasonably high-purity layers, suitable for device applications, can be obtained by a simple bakeout scheme in a clean furnace without addition of H_2O to the growth ambient.

Figure 3.1 illustrates the temperature dependence of the electron mobility in three samples grown after no baking (sample OS-0), 100 hrs In baking (OS-4), and 20 hrs In + 20 hrs melt baking (OS-7). The significant improvement upon baking the entire melt is clear. The solid lines indicate theoretical fits to the experimental data using Matthiessen's Rule and considering ionized impurity, alloy, polar optical phonon and space charge scattering mechanisms. The equations and the constant material

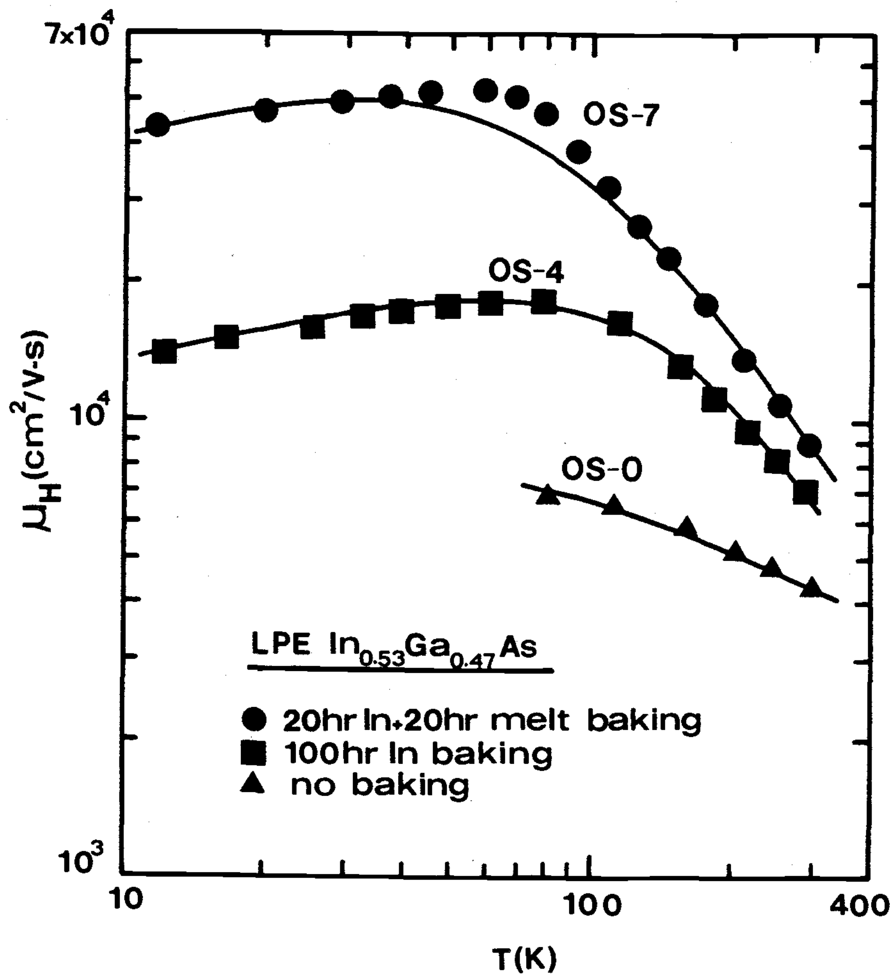

Figure 3.1 Temperature dependence of the Hall electron mobility in LPE $In_{0.53}Ga_{0.47}As$ layers of varying purity. The solid lines indicate the theoretically calculated mobilities.

parameters used for analyzing the data are listed in Appendices I and II, respectively. The values of N_D obtained for samples OS-0, OS-4 and OS-7 are 7.0×10^{16}, 6.8×10^{15}, and 2.4×10^{14} cm^{-3}, respectively, and the values of N_A in the same samples are, 4.7×10^{16}, 3.8×10^{15}, and 1.8×10^{14} cm^{-3}, respectively. The results demonstrate that both donor- and acceptor-like residual impurities are removed by baking In and the entire melt.

3.1.2 Photoluminescence (PL) Measurements

Photoluminescence (PL) spectra of the LPE epitaxial layers at 4.4 K and higher temperatures were recorded for various excitation intensities. The samples were mounted in a strain-free manner in a liquid He cryostat. Excitation was provided by the 6470 A line of a Spectra-Physics Model 171 krypton-ion laser. The incident power was varied, when necessary, by neutral density filters. The incident power density on the sample surface varied from 2.8×10^{-3} to 2.3×10^{-1} W/cm^2. The luminescence was analyzed by a 1m scanning monochromator with a resolution ≤ 1.6 Å and was detected by a liquid nitrogen cooled Ge p-i-n detector. The signal was amplified by a lock-in amplifier and recorded.

3.1.3 PL Spectra Results and Discussion

The general nature of the PL spectra obtained from the LPE samples is shown in Fig. 3.2. The spectra from four samples at

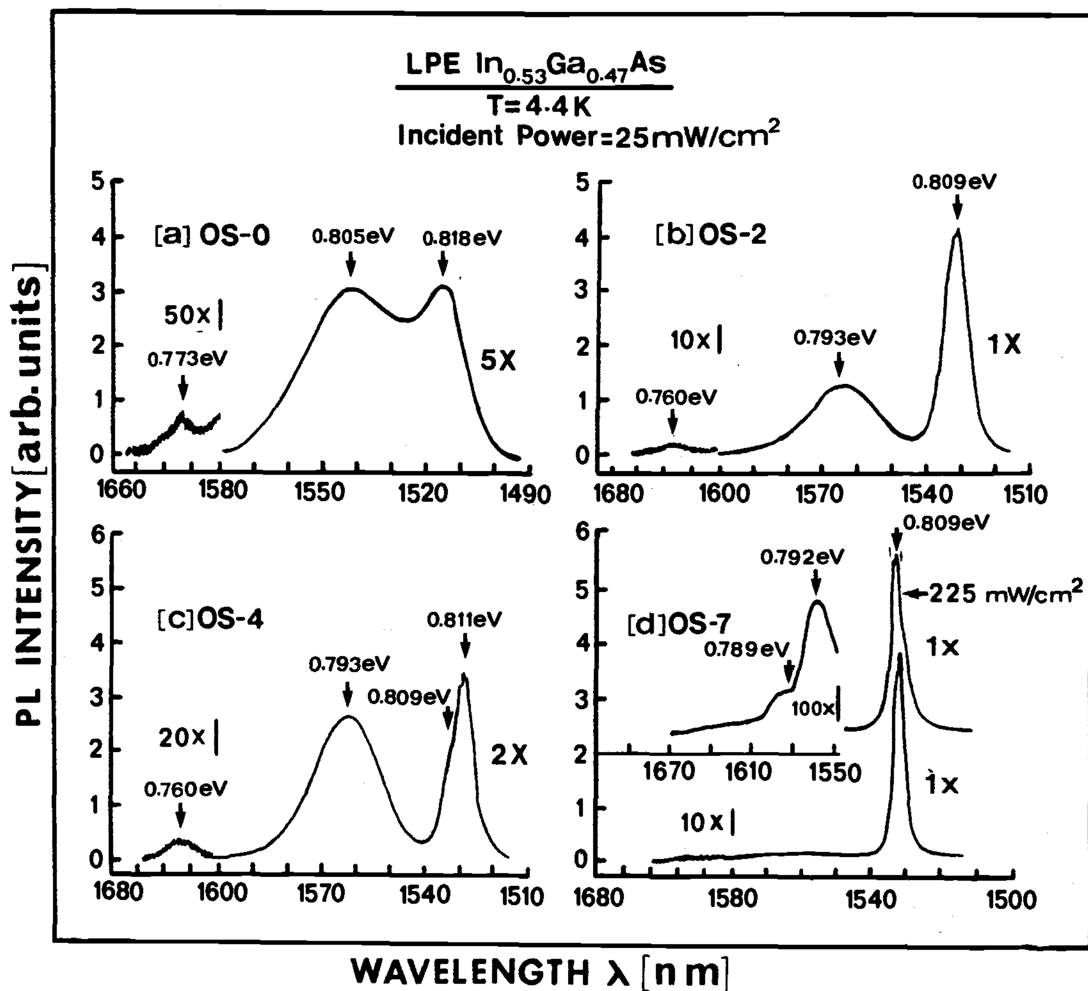

Figure 3.2 Edge photoluminescence observed at 4.4 K for four crystals in increasing order of purity.

4.4K, grown after no baking and different durations of In and melt baking, have been depicted. The three peaks which are characteristic of the spectra are at 1531 nm (0.810 eV), 1562 nm (0.794 eV) and 1629 nm (0.761 eV). It may be reiterated that the general character of the spectra is similar to those reported by Ohno et al.[24] for undoped LPE, and Wicks et al.[25] for MBE $In_{0.53}Ga_{0.47}As$. A slight shoulder to the lower energy side of the 0.810 eV peak has been observed in samples grown after 100 hrs of In or melt baking. The PL intensity of the 0.81 eV peak increases, in general, with increasing purity of the crystal. The intensity of the second peak at 1562 nm remains almost constant without or with In baking alone, but is drastically reduced when the entire growth solution is baked subsequent to baking the In. The third peak at 1629 nm (4.4K) is always observed whenever the peak at 1562 nm is observed.

The peak centered at 1531 nm in the 4.4K spectra with the full width at half maximum, FWHM = 3 - 6 meV is usually not one peak but consists of several transitions. This is evident from Fig. 3.2(d) in which the spectra for the high-purity sample OS-7 are shown for two excitation intensities. At least three transitions are evident. It is, therefore, believed that the overall structure of this peak is made up of several donor-bound (D-X) and acceptor-bound (A-X) excitonic transitions. A shoulder and tail to the main peak (1531 nm) at higher energies appears at 1513 nm (0.819 eV) for T = 30K as shown in Fig. 3.3. This is a

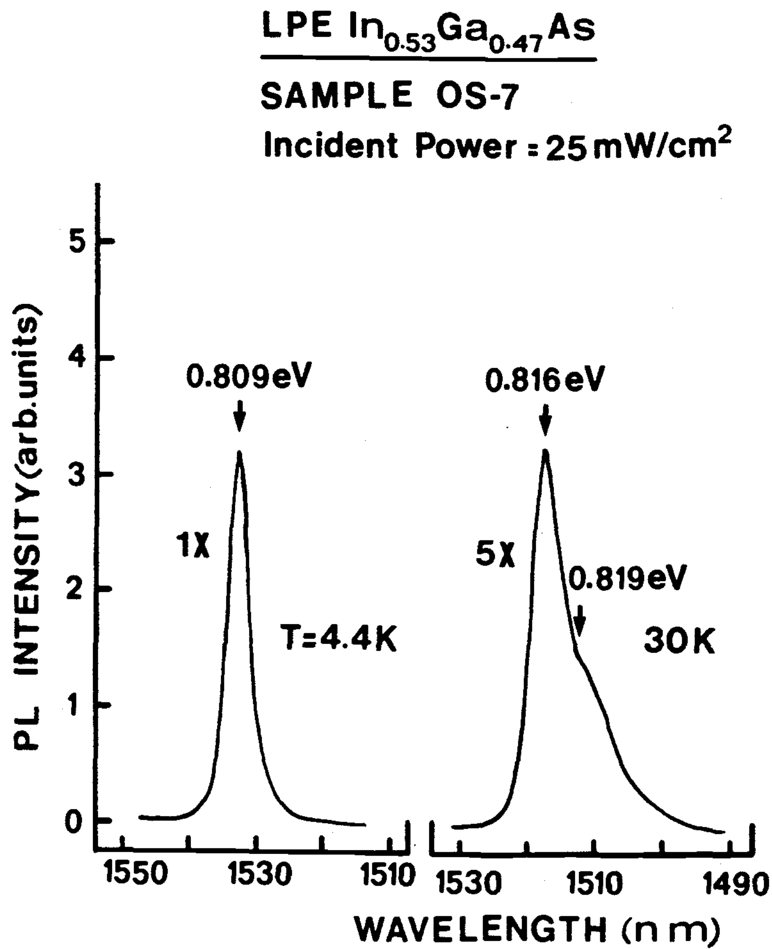

Figure 3.3 Variation in the character of the main peak with temperature in the edge luminescence of sample OS-7.

consistent feature in the spectra of high-purity samples and indicates the onset of transitions involving free excitons. The exciton binding or Rydberg energy E_{ex} is given by

$$E_{ex} = 13.6(\mu/m_o)/\varepsilon_s^2 \text{ (eV)} \qquad (3.1)$$

where μ is the reduced exciton mass and ε_s is the static dielectric constant. Taking an electron effective mass ratio $m_e*/m_o = 0.041$[1] or 0.034[19] and $m_{hh}*/m_o$ and $m_{lh}*/m_o = 0.47$ and 0.05, respectively[20], values of $E_{ex} = 2.0$ or 2.5 meV are obtained. The fundamental bandgap E_G in $In_{0.53}Ga_{0.47}As$ is therefore obtained as 0.821 eV at 30K. The bandgap at 0K is probably 0.822 eV, considering a normal temperature dependence in accordance with the Varshni equation[46].

A very weak transition has been observed at lower energies to the main peak for samples grown after 60-100 hrs of In or melt baking. In Fig. 3.2(c), this feature is indicated by an arrow at 0.809 eV. It is believed that donor-to-acceptor (DA) and free-to-bound (FB) transitions involving C acceptors are responsible for the spectral feature. Carbon is possibly incorporated in the melt from the graphite boat. The binding energy E_A of C acceptors is obtained as 13.0 ± 1.0 meV averaged over several samples[47].

From Fig. 3.2, it is evident that the intensity of the relatively broad second peak at 1562 nm (0.794 eV) in the 4.4K spectra decreases rapidly upon additional baking of GaAs and InAs added to the melt In. It is, therefore, likely that the peak

originates from residual impurities in these compounds, which are removed during baking. Since no change in the spectral features of the transition is noticed at higher temperatures or excitation intensities, it is very likely that the 1562 nm line is due to band-to-acceptor (BA) and (DA) transitions, but predominantly due to the former. The uncertainty partly arises from the small donor binding energies.

The position of the BA emission peak energy in terms of the acceptor binding energy is then given by

$$h\nu = E_G - E_A + kT/2 \qquad (3.2)$$

where transitions involving phonons are excluded. From the spectra of several samples and using E_G (4.4 K) = 0.822 eV, a value of $E_A = 28.0 \pm 1.0$ meV is obtained for the acceptor giving rise to the peak at 1562 nm.

Zn is the most common acceptor impurity which can be incorporated more easily in the growing LPE layer due to its high vapor pressure. The dominant sources of this impurity are InAs and GaAs since extensive baking of these compounds in the melt reduces the corresponding PL intensities to very low values. The position of the 0.794 ± 0.001 eV peak in the PL spectra at 4.4 K is coincident with that in Zn-doped LPE $In_{0.53}Ga_{0.47}As$ (Fig. 3.14). It is, therefore, believed that this peak arises from Zn impurities.

Finally, the very weak transition at 1629 nm, whose intensity varies with that of the peak at 1562 nm, which has been

attributed to Zn is discussed. The average energy separation over several samples is 32.0 ± 1.0 meV. Considering the LO-phonon energy values 32.0 - 34.0 meV in $In_{0.53}Ga_{0.47}As$ determined by several authors[48-50], it is believed that the transition at 1629 nm is an LO phonon replica of the transition involving Zn impurities.

3.2 Postgrowth Heat-Treatment Effects in High-Purity LPE $In_{0.53}Ga_{0.47}As$

The epitaxial layers were annealed in the reaction tube at 670°C for 20 min with a polished InAs proximity cap to prevent As evaporation. It was found that the electrical properties of the layers grown after In baking alone remained almost unchanged, as depicted in Fig. 3.4. On the other hand, mobilities in the layers grown after In and melt baking were, in general, drastically reduced to values close to 3000 cm^2/V.s. The resistivities measured in these heat-treated layers were high, and Hall measurements could not be performed below 260 K.

High-resolution photoluminescence measurements were made on heat-treated samples at 4.4 K. The typical change in the photoluminescence spectra is depicted in Fig. 3.5, where it is evident that the overall luminescence intensity in the range 1510-1700 nm decreases upon heat treatment. This is probably due to additional deep nonradiative impurities created during the heat treatment.

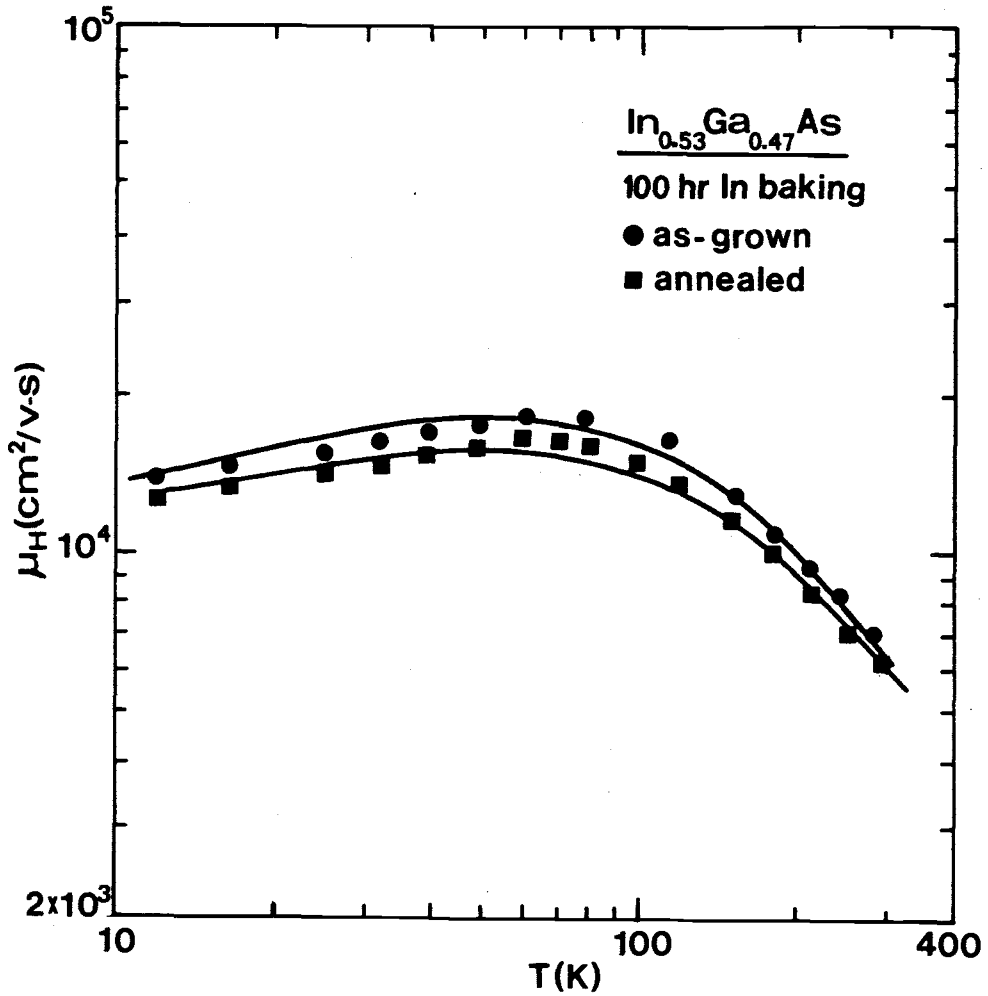

Figure 3.4 Variation of Hall mobility in as-grown and heat treated samples of LPE $In_{0.53}Ga_{0.47}As$ grown after extended baking of In melt alone.

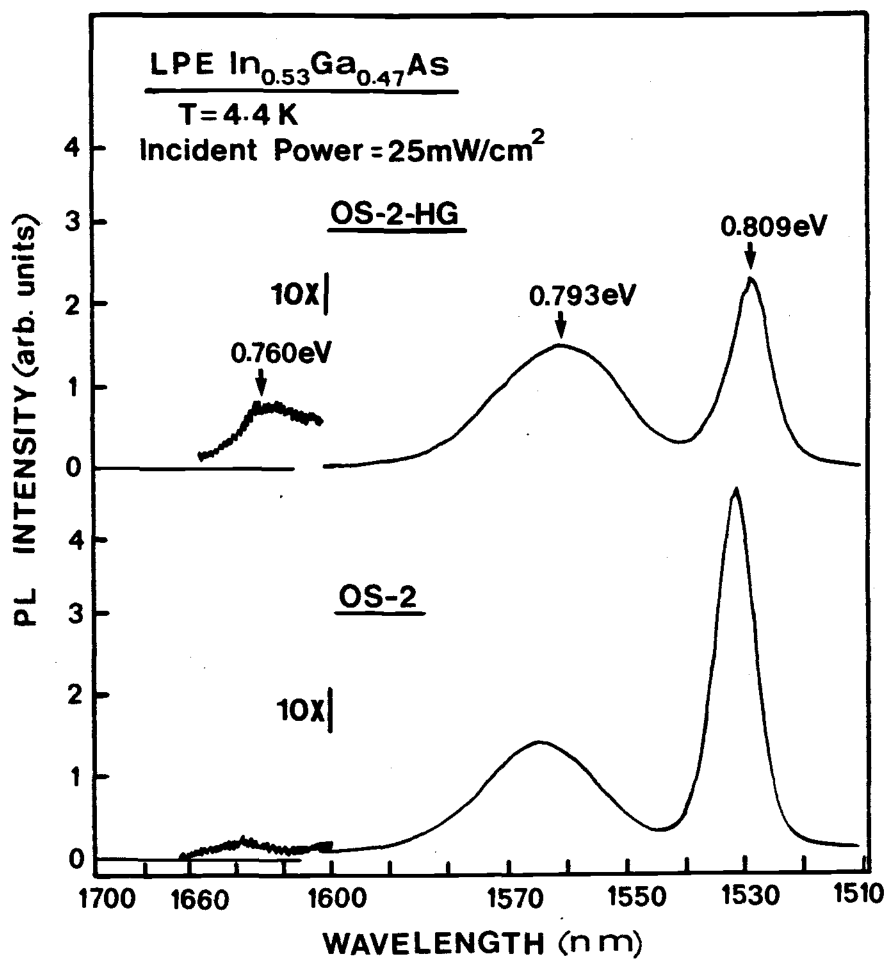

Figure 3.5 Photoluminescence spectra of as-grown and heat-treated $In_{0.53}Ga_{0.47}As$.

Hall measurements were made at higher temperatures on the heat-treated samples which exhibited high resistivity. The variation of n_H with inverse temperature in one such sample is depicted in Fig. 3.6, where similar data from the corresponding as-grown sample have also been included for comparison. It is evident that a deep level is present in the heat-treated sample. An activation energy of 0.18 eV is obtained from the slope of the data points. It is believed that this deep level arises from the out-diffusion of Fe from the InP:Fe substrate[51].

3.3 Characterization of Fe and Cr Doped $In_{0.53}Ga_{0.47}As$

3.3.1 Electrical Properties

Contacts to the samples for Hall measurements were provided by evaporation and alloying of Au-Ge. Figure 3.7 depicts the measured variation of net donor density ($N_D - N_A$) at room temperature with X^1_{Fe} in epitaxial layers grown at 647°C. For $X^1_{Fe} \sim 3 \times 10^{-4}$, we have consistently achieved a low free -carrier concentration, contrary to the observations of Clawson et. al.[22]. For lower values of X^1_{Fe}, it was not possible to achieve reproducibility due to variations in the residual impurity concentration. The measured Hall mobilities and electron concentrations in a representative batch of Fe-doped samples are given in Table 3.2. The decreasing electron mobility with increasing X^1_{Fe} is due to increased impurity scattering.

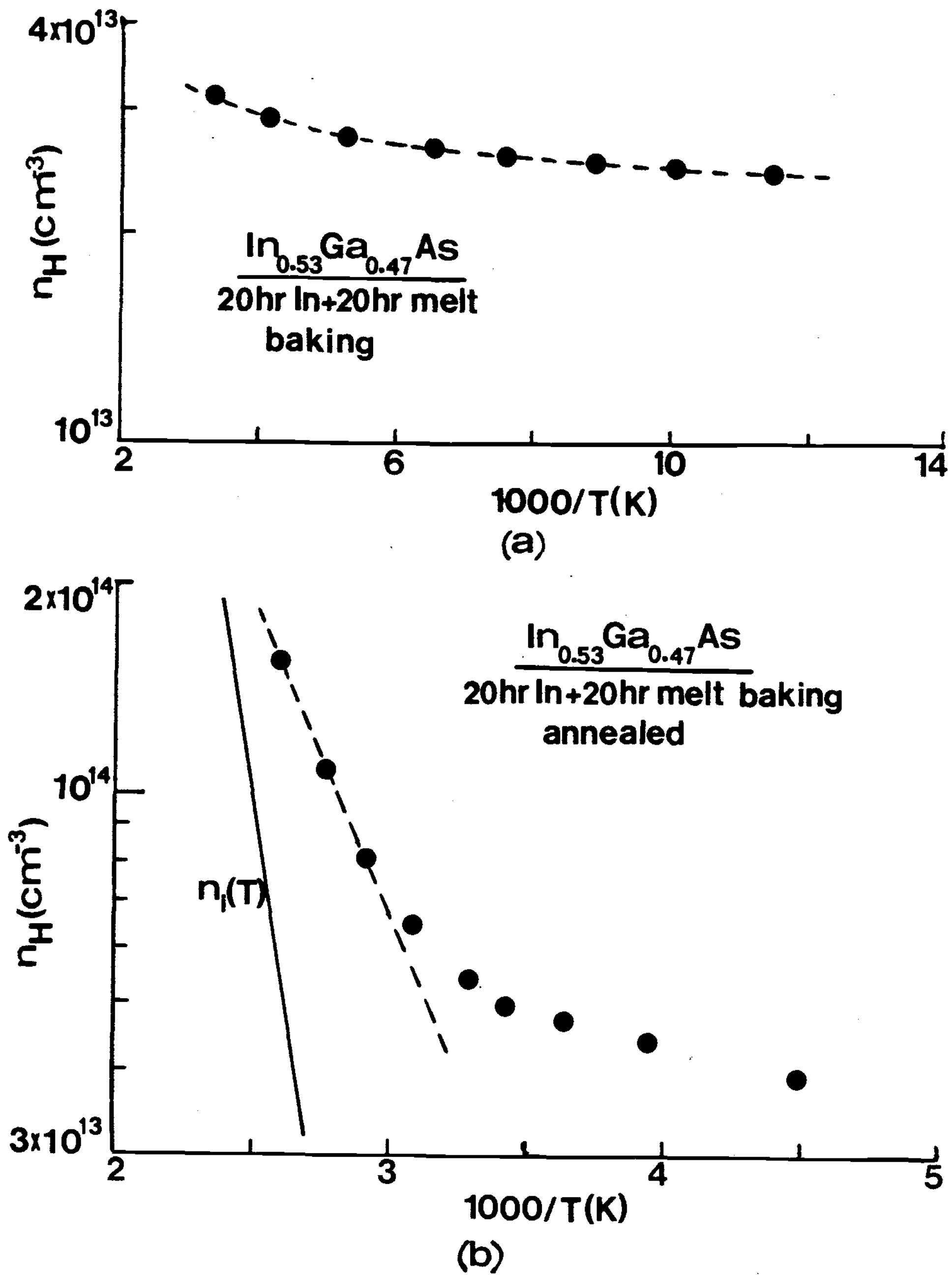

Figure 3.6 Variation of Hall electron concentration in LPE $In_{0.53}Ga_{0.47}As$ (a) before and (b) after heat treatment.

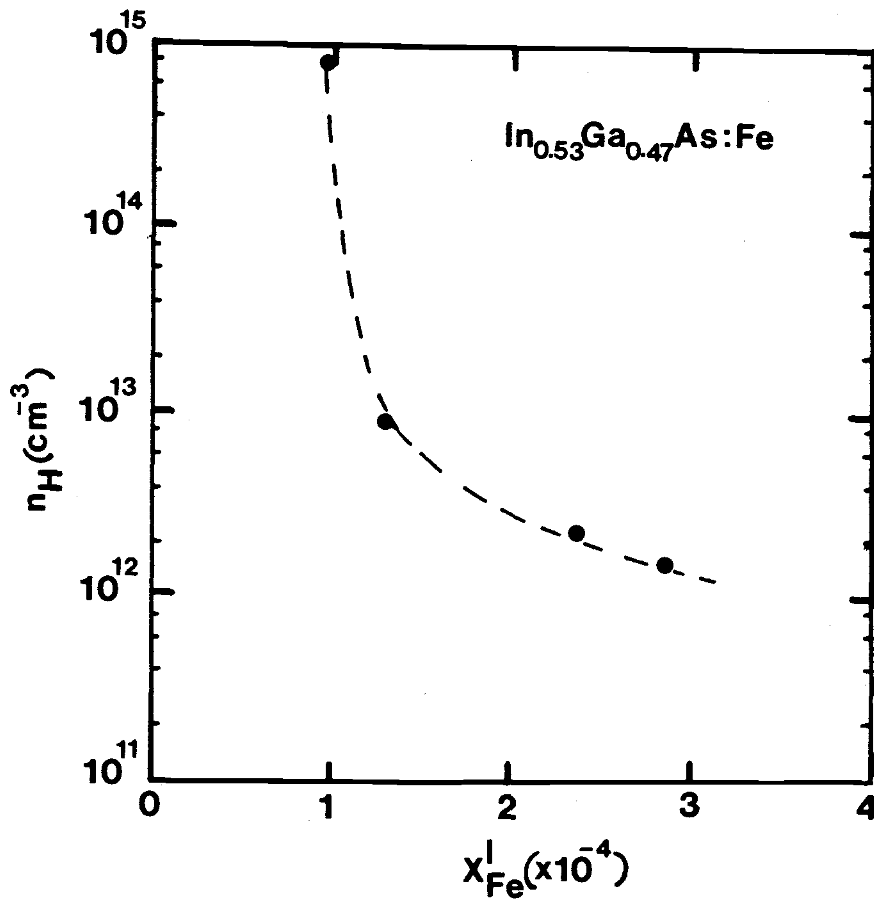

Figure 3.7 Variation of Hall electron concentration at room temperature with X^l_{Fe} in LPE $In_{0.53}Ga_{0.47}As$.

Table 3.2 Electrical Properties of Fe-doped LPE $In_{0.53}Ga_{0.47}As$

Sample	X_{Fe}^{l} $(x10^{4})$	μ_H at 300K $(cm^2/V.s)$	n_H at 300K (cm^{-3})	Resistivity $(\Omega\text{-cm})$
IF0	0	10,200	$1.2x10^{15}$	0.52
IF1	1.0	7,200	$8.0x10^{14}$	0.997
IF2	1.34	6,750	$8.7x10^{12}$	106.9
IF3	2.4	6,400	$2.6x10^{12}$	479.7
IF4	2.9	5,800	$1.8x10^{12}$	608.9

Temperature-dependent Hall measurements were made on some Fe-doped samples. The variation of n_H with inverse temperature for sample IF3 is shown in Fig. 3.8. The data indicate the presence of a deep level in the doped crystal. The electron concentration in a semiconductor containing a deep compensating acceptor level in addition to shallow donor and acceptor levels can be expressed as[52]

$$n = \frac{g_{AA}N_c}{\left[\dfrac{N_{AA}}{N_D - N_A} - 1\right]} \exp\left[-\frac{(E_G - E_{AA})}{KT}\right] \tag{3.3}$$

where E_{AA}, N_{AA} and g_{AA} are the ionization energy, density and spin degeneracy, respectively, of the deep acceptor and N_D and N_A are the shallow donor and acceptor concentrations, respectively. The other symbols in Eqn. 3.3 have their usual meanings. The solid line in Fig. 3.8 indicates the concentration profile obtained by using Eqn. 3.3. From such fitting, values of $E_G - E_{AA}$ = 0.28 eV and $N_{AA}/(N_D - N_A) = 5$ are obtained.

Values of N_D and N_A were determined from analysis of temperature-dependent Hall mobility in undoped samples grown with an identical melt-baking scheme. Assuming that the value of N_{AA} derived above is close to the actual concentration of Fe in the

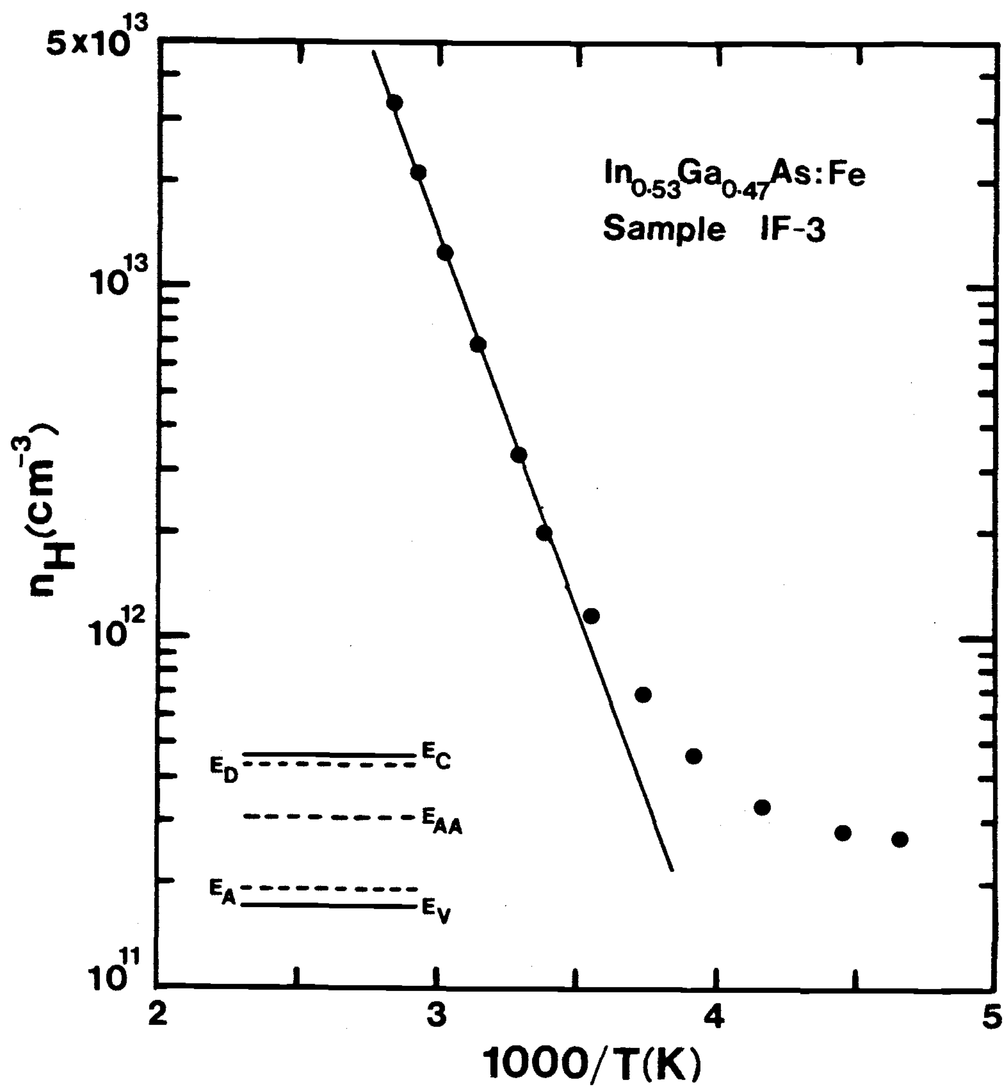

Figure 3.8 Variation of Hall electron concentration with inverse temperature in Fe-doped LPE $In_{0.53}Ga_{0.47}As$.

layer, a value of the distribution coefficient of Fe in $In_{0.53}Ga_{0.47}As$, $C^{S}_{Fe}/C^{l}_{Fe} = 0.0027$ is obtained.

Similar measurements made on the Cr-doped layers have yielded results contrary to the expected behavior. It is observed that in epitaxial layers grown with a melt-baking scheme identical to that for the Fe-doped layers, the free electron concentration increases with X^{l}_{Cr}. The data are listed in Table 3.3, from which it is clear that n_H increases rapidly at first and then saturates for increasing X^{l}_{Cr}. A possible cause for this behavior is discussed later.

The temperature dependence of Hall mobility in two layers doped with different amounts of Cr are shown in Fig. 3.9. The solid lines indicate theoretically calculated mobilities considering ionized impurity, polar-optical phonon, alloy, space-charge, piezoelectric and deformation potential scattering and using Matthiessen's rule. It should be mentioned that the last two scattering mechanisms play a relatively insignificant role in limiting carrier mobilities in the ternary alloy. The material parameters used in the analysis are identical to those in Appendix II. Values of N_D obtained from the analysis for samples IC1 and IC2 are 2.4×10^{15} and 1.5×10^{16} cm^{-3}, respectively, and values of N_A in the same samples are 1.5×10^{15} and 6.0×10^{15} cm^{-3}, respectively. The variation of n_H with inverse temperature in Cr-doped sample is depicted in Fig. 3.10. It is apparent that electrons freeze out into a non-shallow level as the temperature

Table 3.3 Electrical Properties of Cr-doped LPE $In_{0.53}Ga_{0.47}As$

Sample	X^{l}_{Cr} ($\times 10^4$)	μ_H at 300K ($cm^2/V.s$)	n_H at 300K (cm^{-3})
IC1	2.88	8,000	1.5×10^{15}
IC2	4.32	6,975	1.4×10^{16}
IC3	6.67	2,700	2.8×10^{17}
IC4	12.80	3,200	3.2×10^{17}

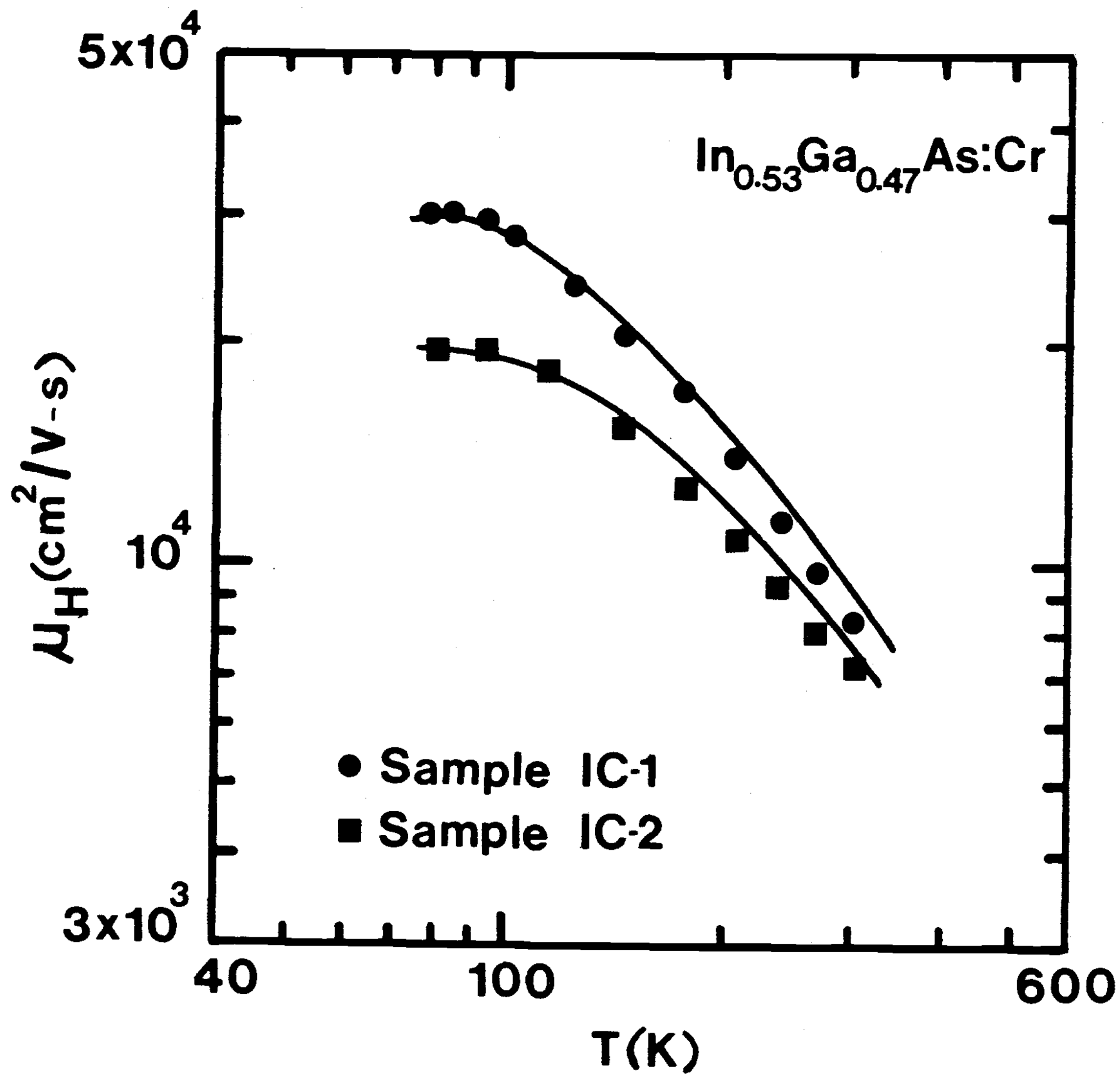

Figure 3.9 Temperature dependence of Hall electron mobility in Cr-doped LPE $In_{0.53}Ga_{0.47}As$.

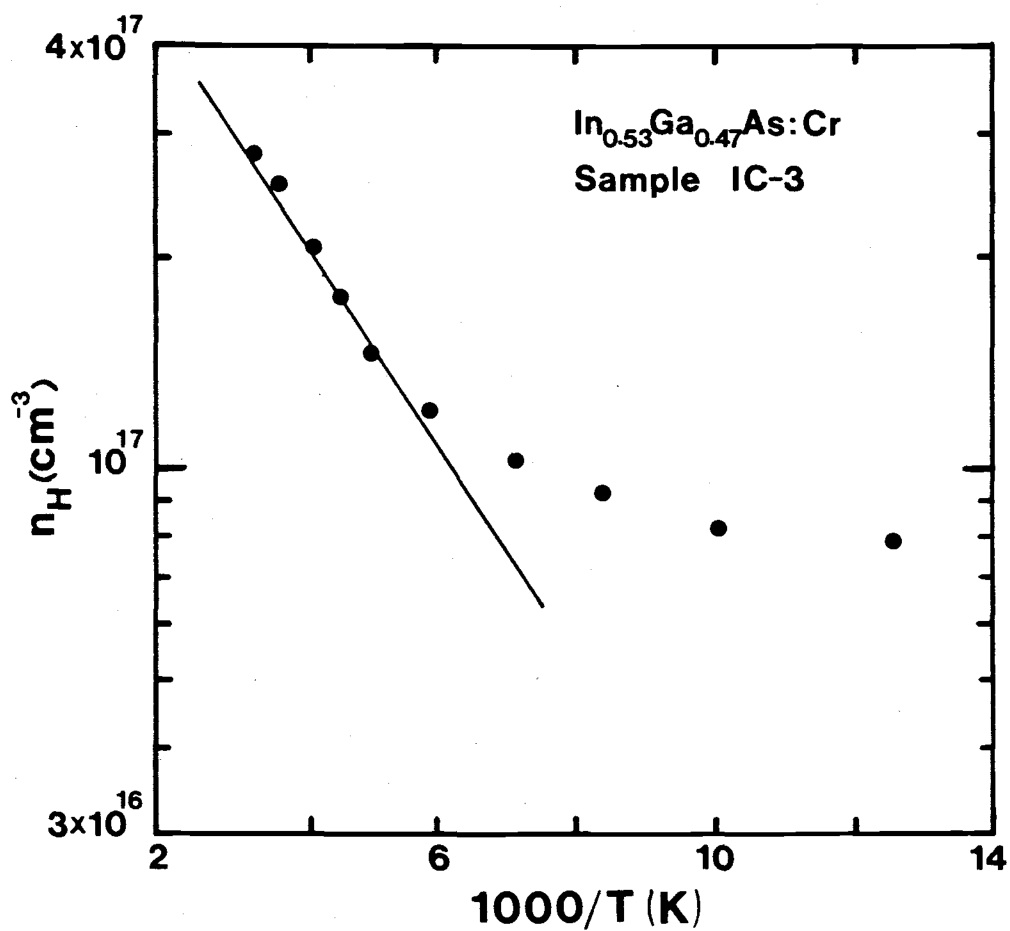

Figure 3.10 Variation of Hall electron concentration with inverse temperature in Cr-doped LPE $In_{0.53}Ga_{0.47}As$.

is lowered. An approximate value of 30 meV is obtained for the ionization energy of this level from the data of Fig. 3.10 and similar data of other Cr-doped samples.

3.3.2 Photoluminescence Measurements on High-Resistivity $In_{0.53}Ga_{0.47}As$

Photoluminescence spectra of Fe and Cr-doped epitaxial layers are shown in Fig. 3.11. The PL spectrum for a high-purity undoped sample is shown in Fig. 3.11(a) for comparison.

The 4.2 K PL spectrum of Fe-doped sample IF-4, containing the largest amount of Fe, is shown in Fig. 3.11(b). It is clear that no new transition due to Fe is present in the near-bandgap luminescence. The spectrum of Cr-doped sample IC-3 is shown in Fig. 3.11(c). A new peak is observed at 1557 nm whose intensity increases with the amount of Cr-added to the growth melt. It is believed that this transition is caused by substitutional Cr or a more complex defect involving Cr.

3.3.3 Discussion

The electrical properties of Fe-doped $In_{0.53}Ga_{0.47}As$ are as expected. The material becomes increasingly resistive with increased addition of Fe to the growth melt. From analysis of the temperature-dependent Hall data, it is evident that Fe introduces a deep level in $In_{0.53}Ga_{0.47}As$ approximately 0.46 eV

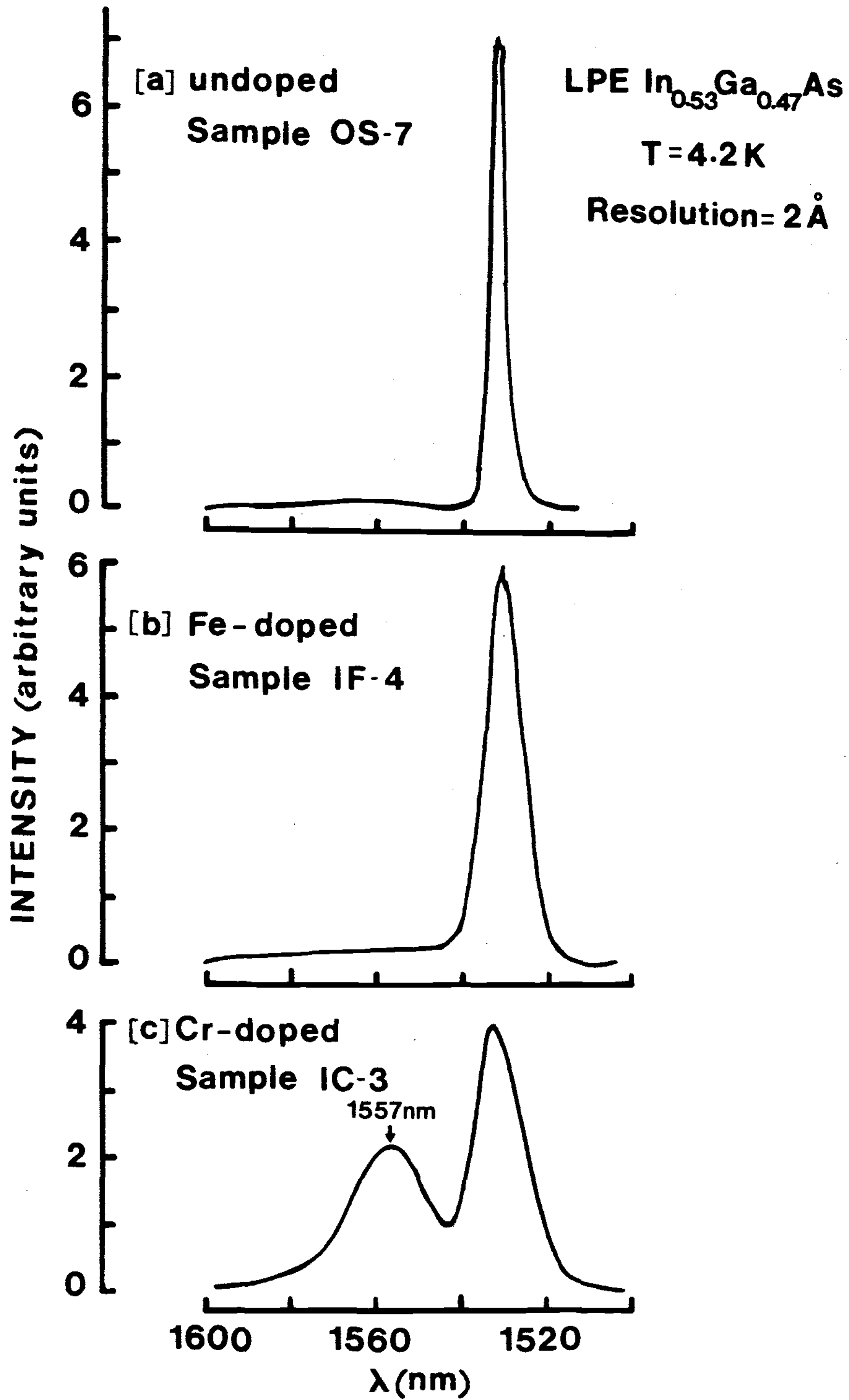

Figure 3.11 Edge photoluminescence observed at 4.2 K for (a) undoped, (b) Fe-doped, and (c) Cr-doped LPE $In_{0.53}Ga_{0.47}As$.

above the valence band edge. Extrapolating from the behavior of Fe in GaAs and InP, it may be concluded that the deep level centers observed in this study behave as acceptors. Low temperature photoluminescence measurements indicate that no new spectral feature is introduced in the edge luminescence by the addition of Fe.

For a carrier concentration $n = 1.5 \times 10^{12}$ cm^{-3}, the energy separation of the Fermi level relative to the conduction band edge, $E_C - E_F$, is 0.298 eV. Since the surface Fermi energy $E_F* = E_{CS} - E_F$ derived from different measurements[53-55] is 0.2 eV, compensated $In_{0.53}Ga_{0.47}As$ has an accumulated surface. This fact has been exploited to make accumulation mode FETs[22,37].

In order to understand the observed behavior of Cr-doped $In_{0.53}Ga_{0.47}As$, it is necessary to recall some earlier observations on the Cr doping of LPE GaAs. Mattes et al.[14] have reported that high-resistivity Cr-doped LPE GaAs can be obtained by the formation of deep levels and the close compensation of shallow donor and acceptor levels. These in turn are dependent on the growth conditions and the growth system components. It was observed by these authors that high-resistivity GaAs layers could be grown only if the pre-growth melt-baking temperature was close to a crucial value of 775°C. It is, therefore, possible that the temperature of 730°C at which the In-Ga-As melts were baked is not the correct value. Otsubo and Miki[15] observed an increase in free-electron concentration of LPE GaAs

grown at 700°C with increase in X^{l}_{Cr}. High resistivity was, however, obtained in layers grown at higher tempertures. They attributed this behavior to the introduction of more oxygen into the melt in the form of oxides of Cr at the lower growth temperatures. Another possibility is the incorporation of S which may be present as a residual impurity in Cr. Sulphur is known to give rise to a shallow donor in $In_{0.53}Ga_{0.47}As$[9, 39]. Andre and Le Duc[56] have grown Cr-doped GaAs by solution growth and have concluded that Cr gives rise to a shallow donor. The same may be true for LPE $In_{0.53}Ga_{0.47}As$. Finally, the formation of a donor-like complex involving Cr and a native-defect cannot be ruled out. The transition in the PL spectra of Cr-doped samples, of energy lower than the bandgap energy by 24.0 meV may very well be due to the donor level. The latter, in turn, could arise from any of the sources outlined above. It is of interest to note that the ionization energy of the deep level derived from temperature-dependent Hall data is also ~ 30meV.

From the values of N_D and N_A derived from the analysis of temperature-dependent mobility data of Cr-doped samples, it is apparent that Cr introduces some amount of auto-compensation. However, with increase of X^{l}_{Cr}, the donor density increases much more than the acceptor density. The extent of this self-compensation must depend on the growth conditions.

3.4 Properties of Zn-Doped $In_{0.53}Ga_{0.47}As$

3.4.1 Electrical Characteristics

The electrical behavior of Zn-doped $In_{0.53}Ga_{0.47}As$ was characterized by Van der Pauw measurements. Ohmic contacts were provided by evaporation and alloying of Au-Zn.

As mentioned in Chapter II, Zn doping was accomplished by the use of Zn-doped GaAs ($N_A - N_D = 1 \times 10^{18}$ cm^{-3}) as a part of the total GaAs in the In-Ga-As growth solution. Typically a 10 hr In bake followed by 10 hr total melt baking has been used to reduce residual ($N_D - N_A$) to approximately 5×10^{15} cm^{-3}.

Figure 3.12 depicts the measured variation of net acceptor density ($N_A - N_D$) at 300° K with X^l_{Zn} in p-type epitaxial layers grown at 647°C. The straight line represents that $N_A - N_D$ is proportional to $(X^l_{Zn})^n$. The value of n in this study is 1.3 which differs from the value of 1.0 reported by Kuphal and Fritzsche (57) for the similar doping technique in $In_{0.53}Ga_{0.47}As$. In heavy doping studies, n is reported as 0.98 by Tashima et al.[58] and as 0.5 by Takeda et al[59] for the ternary alloy. But, Tashima et al.[58] have reported n = 1.35 for their Zn-doping study in the range $2 \times 10^{15} - 6 \times 10^{18}$ cm^{-3} on the quaternary semiconductor. The lowest hole concentration achieved in this study which incidentally is the lowest value reported so far is 2×10^{15} cm^{-3} and the highest RT hole mobility

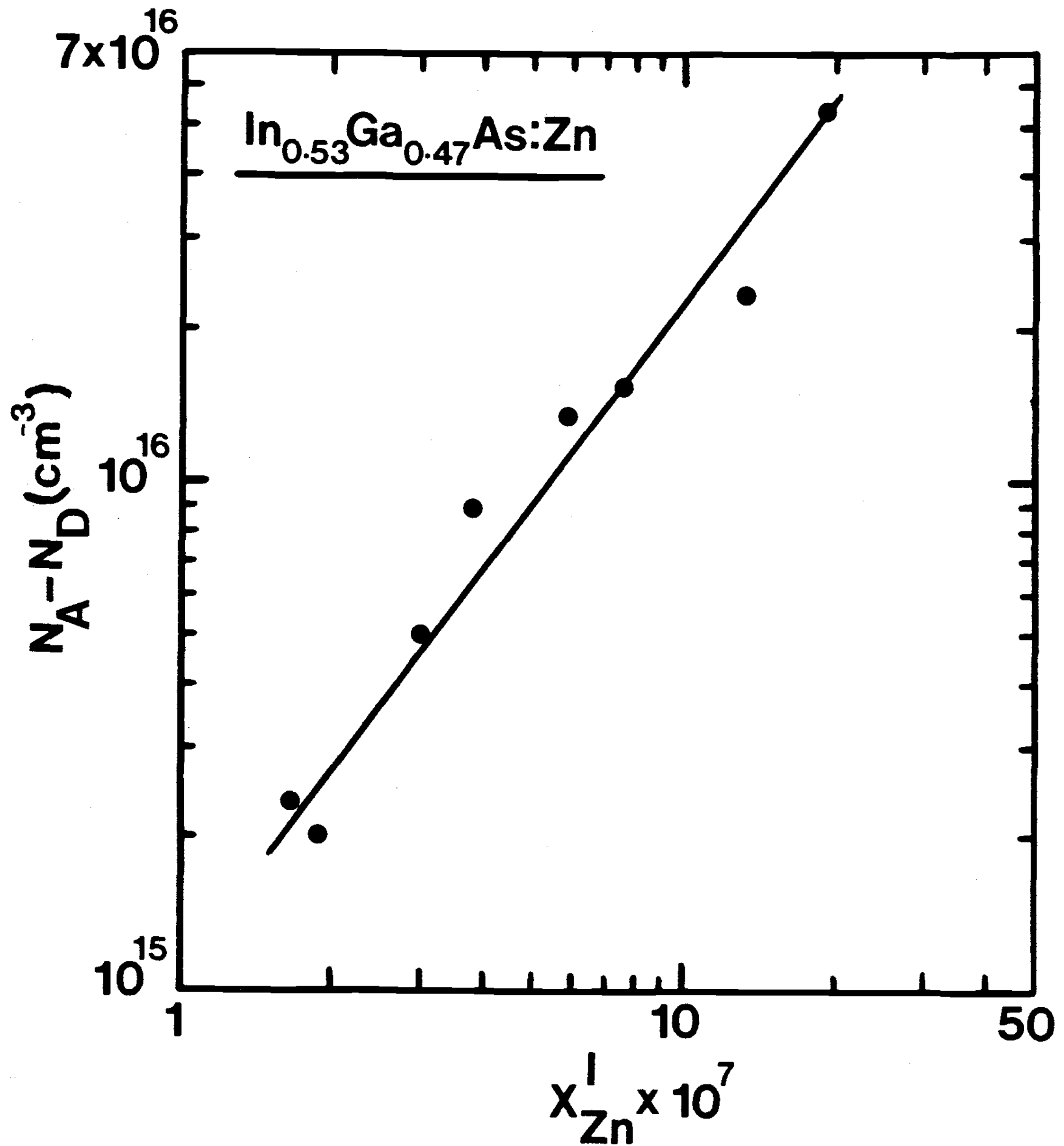

Figure 3.12 Variation of Hall hole concentration at room temperature with X^{l}_{Zn} in LPE $In_{0.53}Ga_{0.47}As$.

is 220 $cm^2/V \cdot s$. By adding maximum possible GaAs:Zn ($N_A - N_D = 1 \times 10^{18}$ cm^{-3}) to the melt, $N_A - N_D$ of 5.3×10^{16} cm^{-3} has been observed in the ternary layers. It is found that the hole concentration is uniform over the entire layer surface. In this study, a series of layers with $(N_A - N_D) \sim 2 \times 10^{15}$ cm^{-3} were grown on (100) InP:Fe substrates for the fabrication of photoconductive detectors. Assuming that the measured free carrier concentration $(N_A - N_D)$ at room temperature is equal to the Zn concentration in the solid, a value of distribution coefficient of Zn in $In_{0.53}Ga_{0.47}As$, $C^s_{Zn}/C^l_{Zn} = 0.77 \pm 0.05$ is obtained. By defining the distribution coefficient k_{Zn} as the ratio of gram atoms of the impurity per gram of solid to that per gram of liquid and using the equation[60]

$$K_{Zn} = \frac{[N_A - N_D]\, A_{In}}{N_L\, \rho\, X^1_{Zn}} \tag{3.4}$$

$$= \frac{3.466 \times 10^{-23}\, (N_A - N_D)}{X^1_{Zn}} \tag{3.5}$$

where A_{In}, N_L and ρ are atomic weight of In, Avagadro's number and the density of the ternary, respectively, $K_{Zn} = 0.52 \pm 0.08$ is obtained which is close to the value reported by Kuphal and Fritzsche[57].

The temperature dependence of hole mobility in samples IZ-7 (X^1_{Zn} = 1.88 x 10^{-7}) and IZ-15 (X^1_{Zn} = 1.92 x 10^{-6}) is shown in Fig. 3.13. The solid lines indicate theoretically calculated mobilities using Matthiessen's rule and considering polar-optical phonon, ionized-impurity, alloy, space-charge, acoustic deformation-potential and non-polar optical phonon scattering mechanisms. The equations used in the analysis for various scattering mechanisms are given in Appendix III and the material parameters used are given in Appendix IV. The values of N_A obtained for samples IZ-7 (X^1_{Zn} = 1.88 x 10^{-7}) and IZ-15 (X^1_{Zn} = 1.92 x 10^{-6}) are 4.3 x 10^{16} and 1.1 x 10^{17} cm^{-3}, respectively, and the values of N_D are 4.05 x 10^{16} and 6.05 x 10^{16} cm^{-3}, respectively. N_D increases with X^1_{Zn} because more residual donor impurities are added to the growth melt with the increased addition of GaAs:Zn which is not subjected to baking.

3.4.2 Photoluminescence Data

The photoluminescence spectrum recorded at 4.2K for Zn-doped sample IZ-9 (X^1_{Zn} = 1.66 x 10^{-7}) is shown in Fig. 3.14. By comparing this spectrum with that of undoped $In_{0.53}Ga_{0.47}As$ given in Section 3.1.2, it is concluded that the peak centered at 1561 nm (0.794) eV arises from band-to-acceptor (BA) and donor-to-acceptor (DA) transitions involving Zn as acceptors.

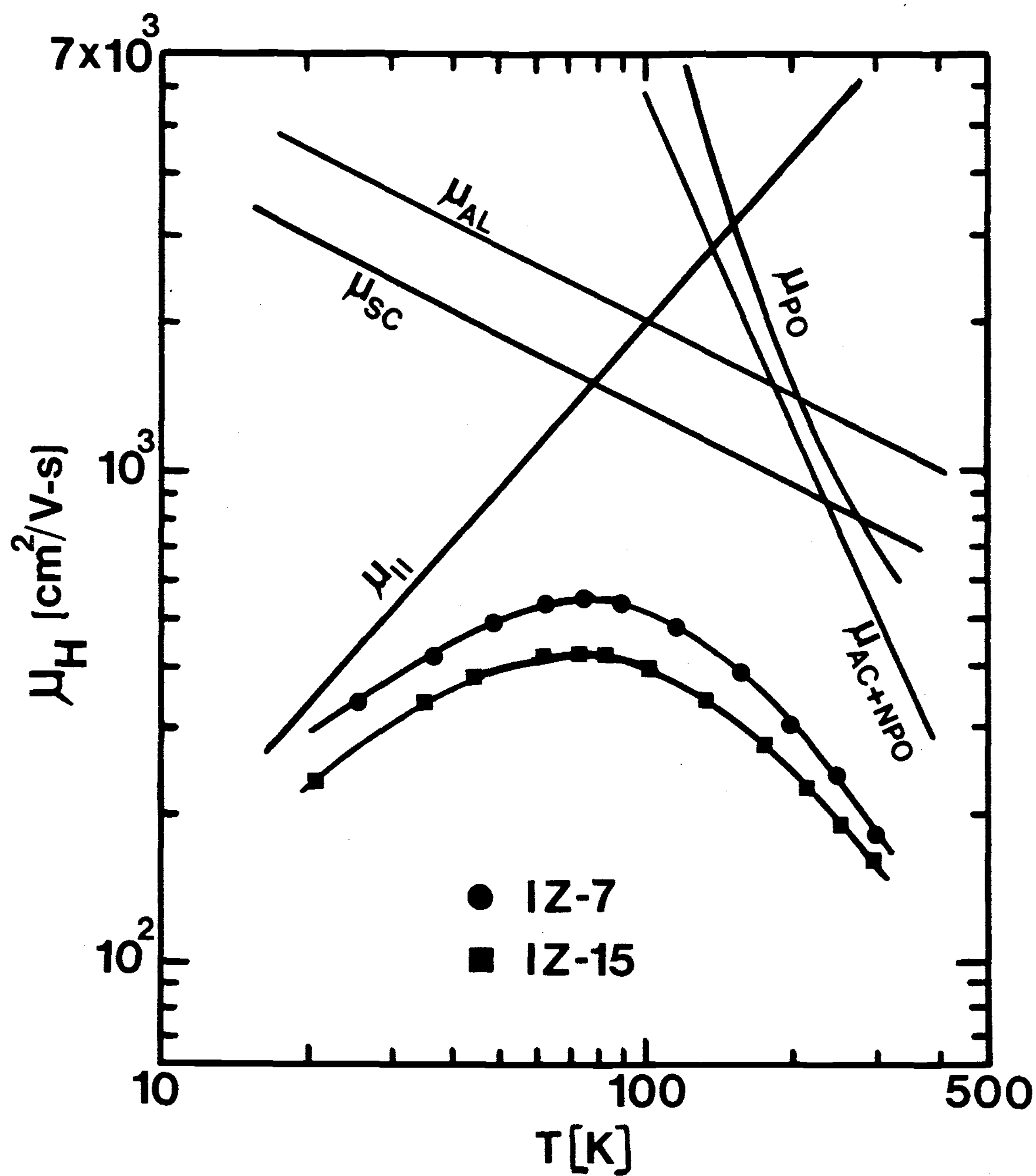

Figure 3.13 Temperature dependence of Hall hole mobility in Zn-doped LPE $In_{0.53}Ga_{0.47}As$.

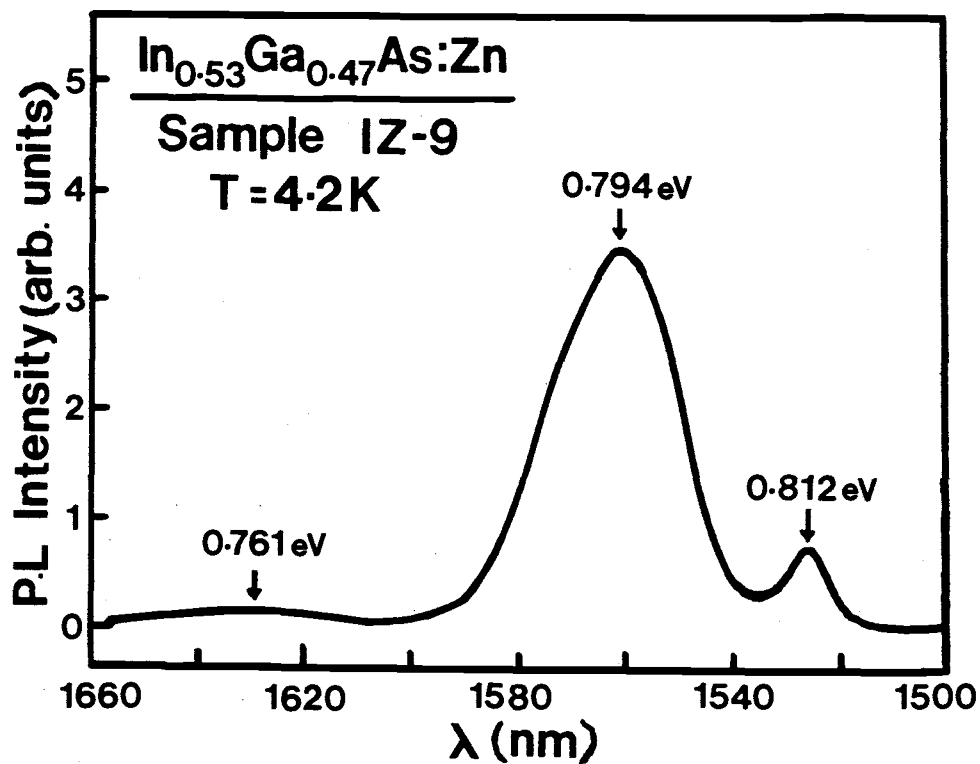

Figure 3.14 Edge photoluminescence spectra of Zn-doped LPE $In_{0.53}Ga_{0.47}As$ at 4.2 K.

3.4.3 Discussion

The behavior of hole mobilities in $In_{0.53}Ga_{0.47}As$ is more complex than that of electrons due to reasons mentioned in Appendix III. In the analysis of temperature-dependent hole mobilities, the $T^{-1/2}$ temperature dependence has been accounted for by considering space-charge scattering and alloy scattering mechanisms. The temperature variation of mobility due to the relevant scattering mechanisms for the sample IZ-7 is depicted in Fig. 3.13. In analyzing hole mobility data, it is observed that acoustic deformation-potential and non-polar optical phonon scattering mechanisms play a more significant role in limiting mobilities at high temperatures. This is markedly different from electron mobilities, which are mainly limited by polar optical phonon scattering at high temperatures. The same feature was observed in the analysis of hole mobility data in germanium-doped p-type $Al_xGa_{1-x}As$[61]. But, this differs from the analysis of hole mobility in InGaAsP as reported by Hayes and Adams[62]. According to their analysis, alloy scattering is the dominant mechanism in the temperature range 80-300K. This probably is the result of not considering space-charge scattering in their analysis. As expected, alloy and space charge scattering mechanisms play an important role in the temperature range 70-250K and ionized impurity scattering limits hole mobility at lower temperatures in $In_{0.53}Ga_{0.47}As$.

CHAPTER IV

THEORY OF PHOTOCONDUCTIVE DETECTORS

In this chapter the types of photoconduction, mechanism of the photoconduction process, photoconductive gain, and the material requirements for photoconductive detectors are discussed.

4.1 Types of Photoconduction

If a material is irradiated with light of a sufficiently short wavelength, so that transitions of carriers occur between valence and conduction bands or between inpurity levels and bands, the conductivity of the material increases. This process is known as photoconduction. There are two types of photoconduction: intrinsic photoconduction and extrinsic photoconduction.

In intrinsic photoconduction, electron transitions occur from the valence band to the conduction band as shown in Fig. 4.1(a). The condition for this type of photoconduction is that the quantum energy:

$$h\nu > E_G \qquad (4.1)$$

The maximum wavelength for the photoconductive effect is therefore

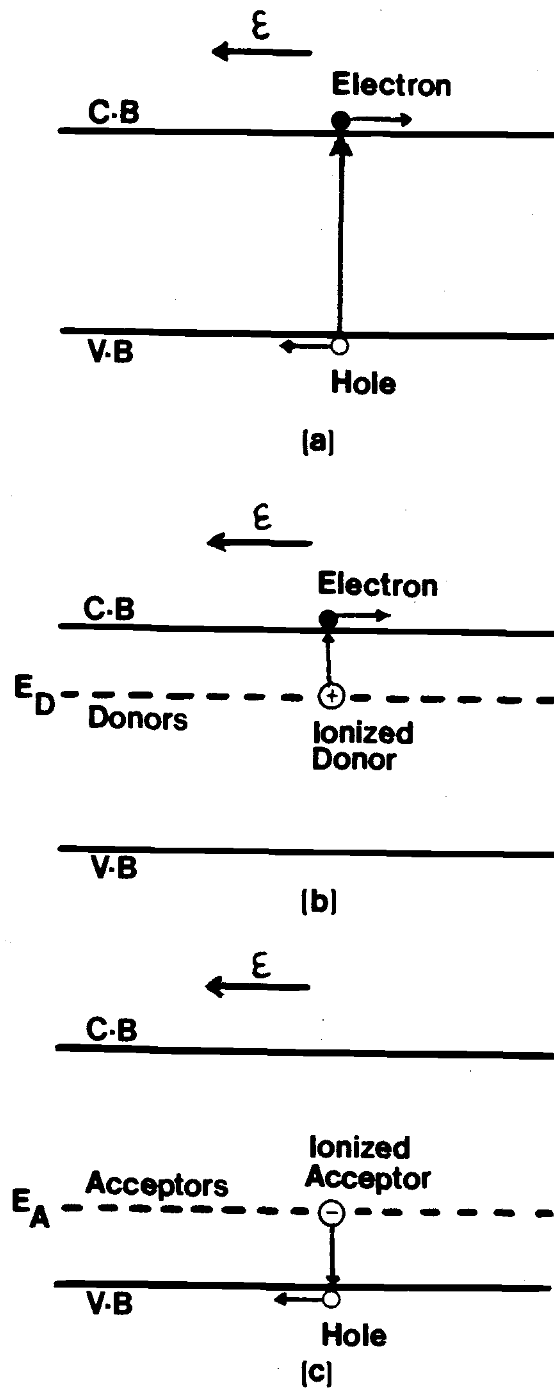

Figuare 4.1 Photoconduction transitions (a) intrinsic, (b) extrinsic involving donor levels and (c) extrinsic involving acceptor levels.

$$\lambda_{max} = \frac{hc}{E_G} = \frac{1.24}{E_G\,(eV)}\ \mu m \tag{4.2}$$

where E_G is the bandgap in electron volts. Eqn. (4.1) is valid for direct bandgap semiconductors, but if the semiconductor is indirect bandgap, intrinsic photoconduction is made possible by phonon-assisted transitions. In intrinsic photoconduction, both free electrons and free holes can contribute to the conduction process.

In extrinsic photoconduction, only one type of carrier contributes to the photocurrent. Consider a semiconductor with a deep-lying donor level at an energy E_D from the bottom of the conduction band. At low temperatures, almost all the electrons are bound to these donor centers and the conductivity is small. If the material is irradiated by light of quantum energy

$$h\nu \geq E_D \tag{4.3}$$

the conductivity of the material increases, because electrons make transitions from the neutral donor levels to the conduction band as shown in Fig. 4.1(b). Similarly, in a semiconductor with a deep acceptor level, low-temperature photoconductivity becomes possible as shown in Fig. 4.1(c) if

$$h\nu \geq E_A \tag{4.4}$$

where E_A is the ionization energy of the acceptors. In this case, free holes are formed when electrons make transitions from the valence band to the neutral acceptors.

4.2 Mechanism of Intrinsic Photoconduction

If the photoconductive sample shown in Fig. 4.2 is irradiated uniformly on its active area, by W watts of light of energy $h\nu$, then the number of electron-hole pairs generated per second is

$$Q = \frac{\eta_i W}{h\nu} \qquad (4.5)$$

where η_i is the internal quantum efficiency of the electron-hole pair generation process.

In order to calculate the increase of carrier concentration by the absorption of light one needs to know the carrier lifetime in the active volume, before they recombine or are swept out. Also, one has to consider injection of carriers through the contacts into the photoconductor. If, for example, an electron is swept out through the anode before a hole, the photoconductor loses negative charge, which has to be replenished by injection from the cathode contact to maintain space-charge neutrality. This goes on until the hole is swept out too, or until recombination occurs. Hence, if electron and hole lifetimes (τ_n and τ_p) are not equal, the photoconductive effect depends on the longer of the two lifetimes. The photoexcited carrier density Δn, which is equal for electrons and holes, is

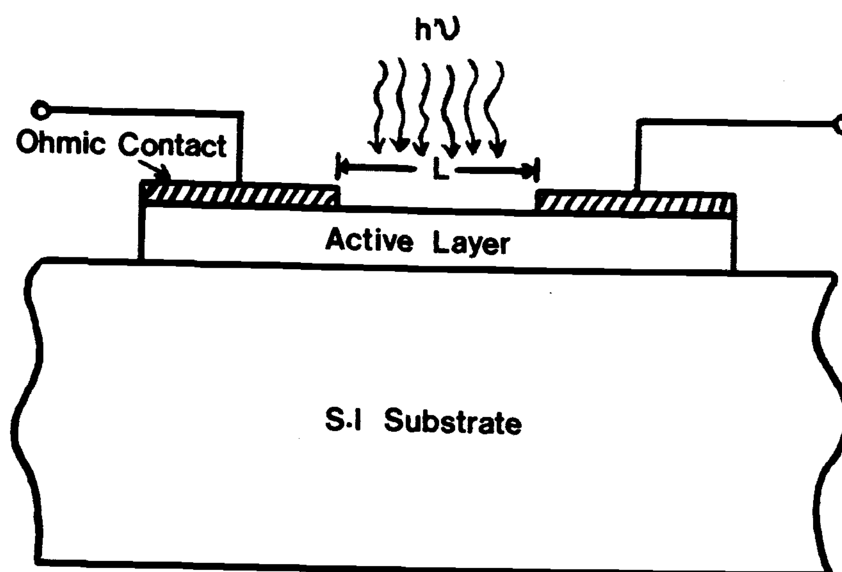

Figure 4.2 Cross-sectional view of a lateral photoconductive detector.

$$\Delta n = \frac{Q \, \tau_{eff}}{V_o} \tag{4.6}$$

where τ_{eff} is the effective carrier lifetime[63] and V_o is the active detector volume. The corresponding photocurrent is[64]

$$I_{ph} = \frac{qVQ \, \tau_{eff} \, (\mu_n + \mu_p)}{L^2} \tag{4.7}$$

where V is the voltage applied to the photoconductive detector, L is the active channel length of the detector, and q is the electronic charge. For sensitive photoconductors, either the mobilities should be large or the effective lifetime should be large, or both. Furthermore, the length L should be small.

4.3 Photoconductive Gain

For any photodetector not having avalanche gain, the photoconductive gain (defined as the number of carriers collected in the external circuit per incident photon) is[63]

$$\Gamma = \frac{h\nu}{q} \frac{I_{ph}}{n_i W} . \tag{4.8}$$

Using equations (4.5) and (4.7) the gain can be expressed as

$$\Gamma = \frac{\tau_{eff}(\mu_n+\mu_p)V}{L^2} \tag{4.9}$$

since $\mu_p \ll \mu_n$

$$\Gamma = \tau_{eff}\,\mu_n \frac{V}{L^2} \tag{4.10}$$

$$= \frac{\tau_{eff}}{t_r} \tag{4.11}$$

where t_r is the transit time of the carrier. Γ can range from values larger than unity for very sensitive photoconductive detectors ($\tau_{eff} > t_r$) to values smaller than unity ($\tau_{eff} < t_r$).

The gain bandwidth product of a photoconductive detector is[63]

$$\Gamma B = \frac{1}{2\pi}(\mu_n+\mu_p)\frac{V}{L^2} \tag{4.12}$$

From Eqns (4.9) and (4.11), it is evident that both gain and gain-bandwidth product can be improved by reducing the channel length L. The internal optical gain of the photoconductive detector is

$$G_{opt} = \frac{h\nu}{q}\cdot\frac{I_{ph}}{W} = \eta_i\Gamma \tag{4.13}$$

$$\simeq \eta_i \tau_{eff} (\mu_n + \mu_p) \frac{V}{L^2} \tag{4.14}$$

$$\simeq \eta_i \frac{\tau_{eff}}{t_r} \tag{4.15}$$

Taking into account surface reflection of the incident light by the reflection coefficient R and incomplete absorption in the active region, the external photoconductive gain is

$$\Gamma_{ext} = (1 - R)(1 - e^{-\alpha d})\Gamma \tag{4.16}$$

where d is the thickness of the active layer and α is the absorption coefficient of the photoconductive material.

4.4 Material Considerations for Photoconductive Detectors

The material requirements for photoconductive detectors are high resistivity and high carrier mobilities and drift velocities. High-resistivity material gives low dark current in the devices which in turn generates low thermal noise and perhaps low $1/f^n$ noise[32]. It also provides device isolation and reduces parasitic device capacitances in integrated optoelectronic circuits. Photoconductive detectors made on semi-insulating GaAs and InP exhibit high response speeds[65,66] due to short carrier life times. The short carrier life time is due to the introduc-

tion of deep levels in the bandgap of the material. The high carrier mobility can yield a short transit time and consequently high gain. Hence, semi-insulating $In_{0.53}Ga_{0.47}As$ is attractive over n and p-type material for photoconductive detector application in the wavelength range 1.2 - 1.7 µm. The room-temperature mobility of 6400 $cm^2/V.s$ measured in the high-resistivity layers used for fabricating devices in this study is excellent. However, an intrinsic problem with such material is that the detector gain might be degraded by the deep Fe acceptor level. To determine the extent of this limitation, if present at all, the optical gain of Fe-doped $In_{0.53}Ga_{0.47}As$ photoconductive detectors is compared with identical devices fabricated on Zn-doped p-type $In_{0.53}Ga_{0.47}As$. It is found that the gain in detectors fabricated in both types of material are comparable.

CHAPTER V

PERFORMANCE CHARACTERISTICS OF $In_{0.53}Ga_{0.47}As$ PHOTOCONDUCTIVE DETECTORS

5.1 Device Fabrication

Photoconductive detectors were fabricated with Fe-doped $In_{0.53}Ga_{0.47}As$ having $(N_D - N_A) \sim 2 \times 10^{12}$ cm^{-3}. The measured Hall mobility at 300K in this material is $\sim$ 6000 $cm^2/V.s$. For comparison purposes devices were also fabricted with Zn-doped p-type $In_{0.53}Ga_{0.47}As$ having $p \sim (2-5) \times 10^{15} cm^{-3}$. The devices are of source-drain and interdigitated configurations with Ni/Au-Ge electrodes having 7 μm spacings. The electrode structures were patterned onto the $In_{0.53}Ga_{0.47}As$ using vacuum evaporation and metal lift-off techniques and were subsequently alloyed at 450°C to form ohmic contacts. An SEM photomicrograph of a typical device is shown in Fig. 5.1(a).

5.2 Dark Current-Voltage Characteristics

Typical dark current-voltage characteristics of non-interdigitated devices on $In_{0.53}Ga_{0.47}As$:Fe are shown in Fig. 5.1(b). The measured currents are about three times larger for interdigitated devices. The source-drain current increases linearly with voltage at first and then shows a trend towards saturation

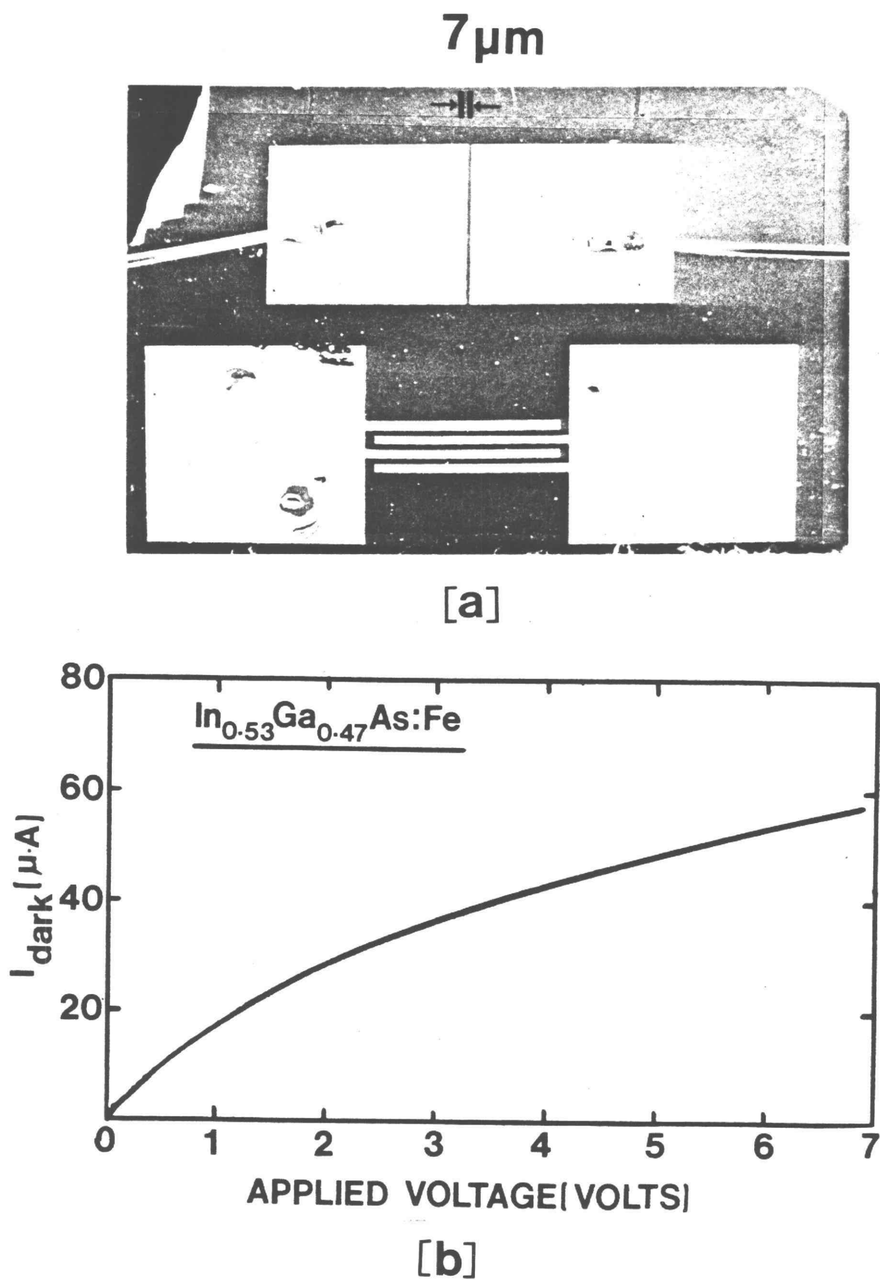

Figure 5.1 (a) SEM photomicrograph of $In_{0.53}Ga_{0.47}As:Fe$ photoconductive detector, (b) dark current-voltage characteristics for a planar source-drain photoconductive detector.

as the electron velocity reaches a peak. But, it does not saturate at any voltage range. Possible reasons for this behavior are surface conduction, conduction through states at the substrate-active layer interface[30] and space-charge injection from the contacts.[67]

5.3 Device Results and Discussion

5.3.1 Spectral Response

The arrangement for spectral response measurements is shown in Fig. 5.2. A Ge p-i-n diode was used for calibrating the measurement system. The spectral response of a $In_{0.53}Ga_{0.47}As$:Fe photodetector at 300 and 77K is shown in Fig. 5.3. The shift of the peak to shorter wavelengths at 77K is due to the increase in bandgap with lowering of temperature. The long wavelength cutoff is determined by the absorption edge of $In_{0.53}Ga_{0.47}As$. The detector also shows response to wavelengths greater than 1.65 μm, which probably is due to the excitation of electrons from the residual acceptor levels to the conduction band. Similar spectral response features were observed for $In_{0.53}Ga_{0.47}As$:Zn photodetectors.

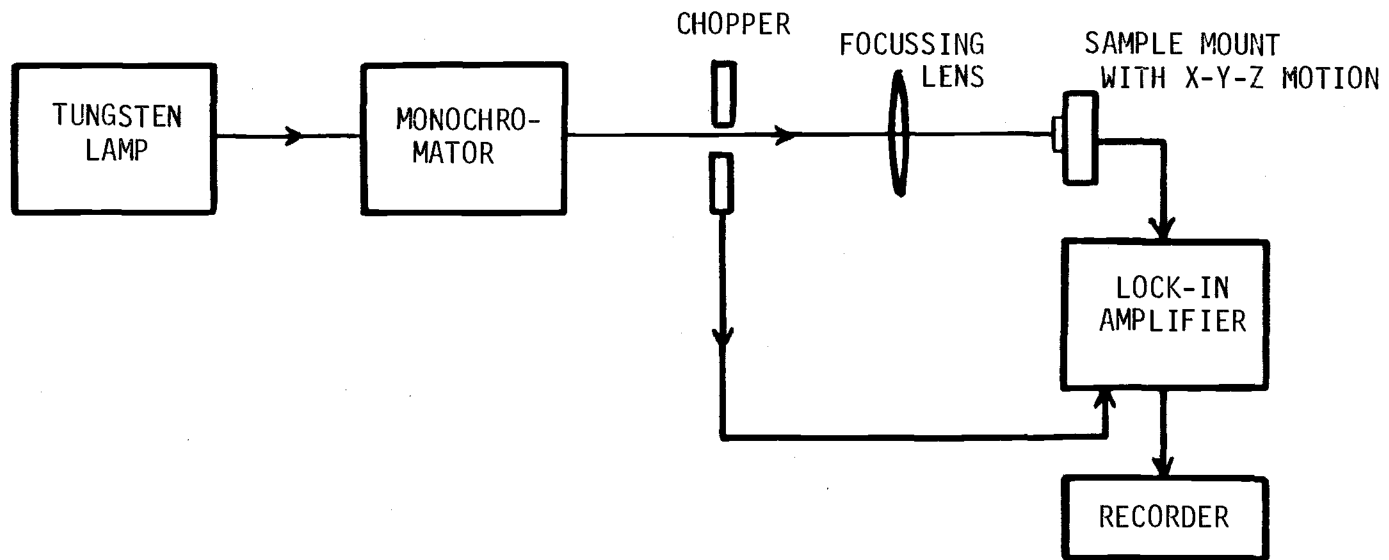

Figure 5.2   Schematic for spectral response measurements.

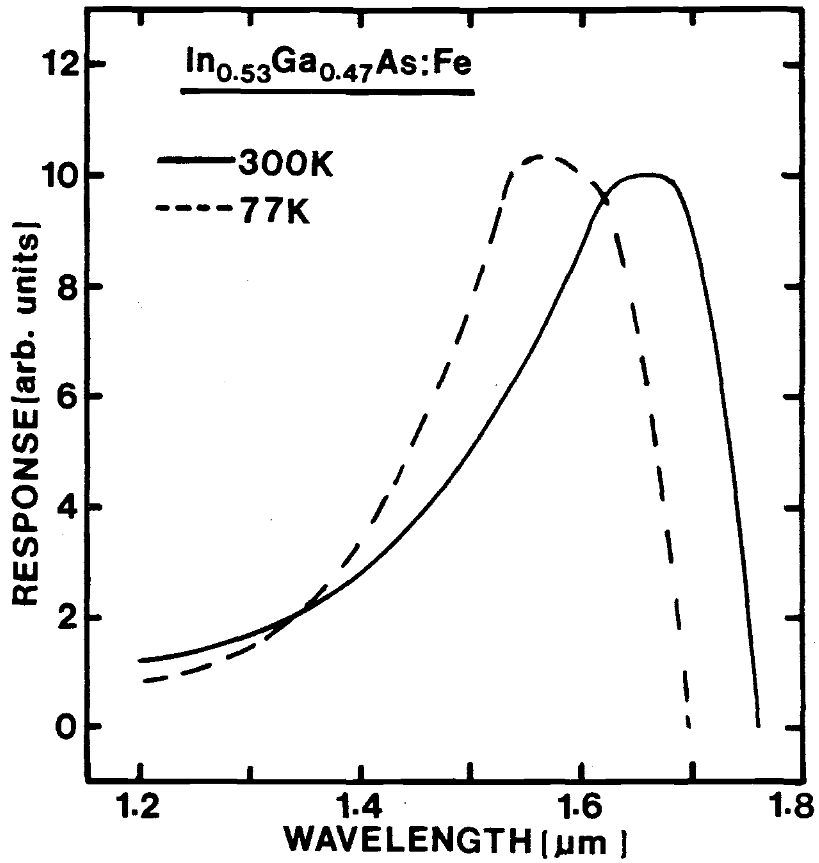

Figure 5.3 Spectral response of $In_{0.53}Ga_{0.47}As:Fe$ photoconductive detector measured at a bias of 2V.

5.3.2 Impulse Response of $In_{0.53}Ga_{0.47}As$:Fe Photodetector

The response speed for a non-interdigitated device mounted on a 50 Ω coaxial stripline was measured using a (GaIn) (AsP) laser emitting at 1.29 μm. The laser was driven by a comb generator resulting in 300 ps or 11 ns (FWHM) light pulses with a a repetition rate of 100 MHz. Fig. 5.4(a) shows the detector response for 300 ps pulses at a bias of 6V. The response is characterized by a rise time t_r of 200 ps, FWHM of 400 ps, and a fall time of 1.0 ns.

The rise time does not represent the true characteristic of the detector. It includes the total effects due to oscilloscope trigger jitter, oscilloscope rise time, optical pulse rise time, signal dispersion in transmission from the device to the sampling head, and RC time constant due to device capacaitance and transmission-line impedance. The long fall time of 1.0 ns is a result of a long tail (~ 3 ns) in the turn-off characteristics and limits the 3dB bandwidth ($1/2\pi t_f$) to ~ 160 MHz. This is an improvement over the fall time of 2.5 ns observed by Chen et al.[32] in the response of devices made on n-type $In_{0.53}Ga_{0.47}As$ with 3.6 m contact spacing 7μm in this study). It is believed that by reducing the contact spacing to 3 μm fall times as small as 500 ps (BW~ 320MHz) can be achieved with $In_{0.53}Ga_{0.47}As$:Fe photoconductive detectors for 300 ps excitation pulses. From Fig. 5.4(b) t_r, FWHM, and t_f of 6 ns, 11.2 ns, and 11ns,

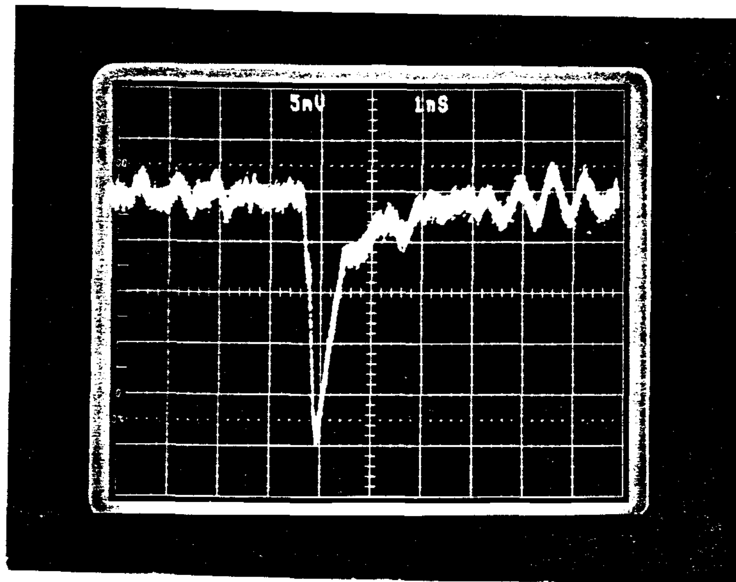

(a)

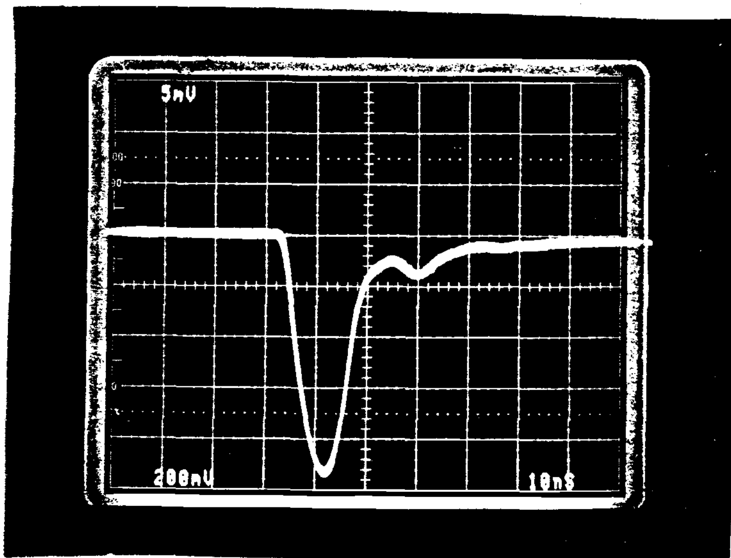

(b)

Figure 5.4 Photoresponse of $In_{0.53}Ga_{0.47}As$:Fe photoconductive detector at 6V bias to (a) 300 ps and (b) 11 ns pulses provided by 1.29μm InGaAsP laser.

respectively, have been observed for 11 ns excitation pulses. The small peaks appearing in Fig. 5.4 are due to impedance mismatch between the stripline mount and the coaxial lines.

Due to gain-bandwidth limitations, the responsivity of photoconductive detectors increases as the optical excitation pulses become broader. From Fig. 5.4, it is observed that for 300 ps and 11 ns excitation pulses, the detector has developed a peak photocurrent of 0.5 and 0.475 mA, respectively. To calibrate the responsivity of the test device, a high-speed, AR-coated $In_{0.53}Ga_{0.47}As$ pin photodiode, which has a diameter of 100 μm, a capacitance < 0.5 PF, and an external quantum efficiency of 90% at 1.29 μm has been used. For the same testing conditions, the photodiode developed peak photocurrents of 0.8 mA and 0.1 mA for 300 ps and 11 ns optical excitation pulses, respectively. As a result,the non-interdigitated device has 0.625 and 4.75 times the responsivity of a p-i-n photodiode for 300 ps and 11 ns pulses, respectively. This implies an equivalent external quantum efficiency of 427% (or a photoconductive gain of 4.27) at λ = 1.29 μm for 11 ns excitation pulses. Reduction of electrode spacing could improve the gain under high speed testing ($\leq$ 300 ps pulses) conditions.

Since the gain of a photoconductive detector is determined by the ratio of carrier lifetime to carrier transit time between the contacts, the response time, which is determined by the carrier lifetime, is proportional to the device gain times the

electron transit time. Using the measured gains of 4.27 and 0.56 and an electron transit time of 35 ps (with 7 μm channel length and an electron drift velocity of 2×10^7 cm/s) the expected response times are 150 ps and 20 ps, respectively, for 11ns and 300ps excitation pulses. By subtracting the FWHM of the excitation pulses from the corresponding measured FWHM of the device responses, values of 200ps and 100ps are derived for the response time with 11ns and 300ps excitation pulses, respectively. The agreement is poor for 300ps pulses, because the device does not truly reach steady-state condition. Other possible causes of this discrepancy are effects on the risetime due to the measurement system and the capture and re-emission of holes from traps at the substrate-active layer interface [30].

Unlike the responsivity of a pin photodiode, that of a photoconductive detector varies considerably with bias voltages. As shown in Fig. 5.5, the responsivity of $In_{0.53}Ga_{0.47}As:Fe$ photoconductive detector for 11 ns pulses, initially increased linearly with bias voltage and then showed a trend towards saturation at higher voltages as expected from v-E behavior. However, the responsivity does not saturate above the critical field of $E_c \sim 3$ KV/cm. An inner amplification mechanism induced by avalanche effects facilitated in the narrow bandgap ternary alloy might be responsible for this behavior[31]. The response broadening effect observed at lower bias voltages in modulation doped heterostructure devices [34] is not seen in this study.

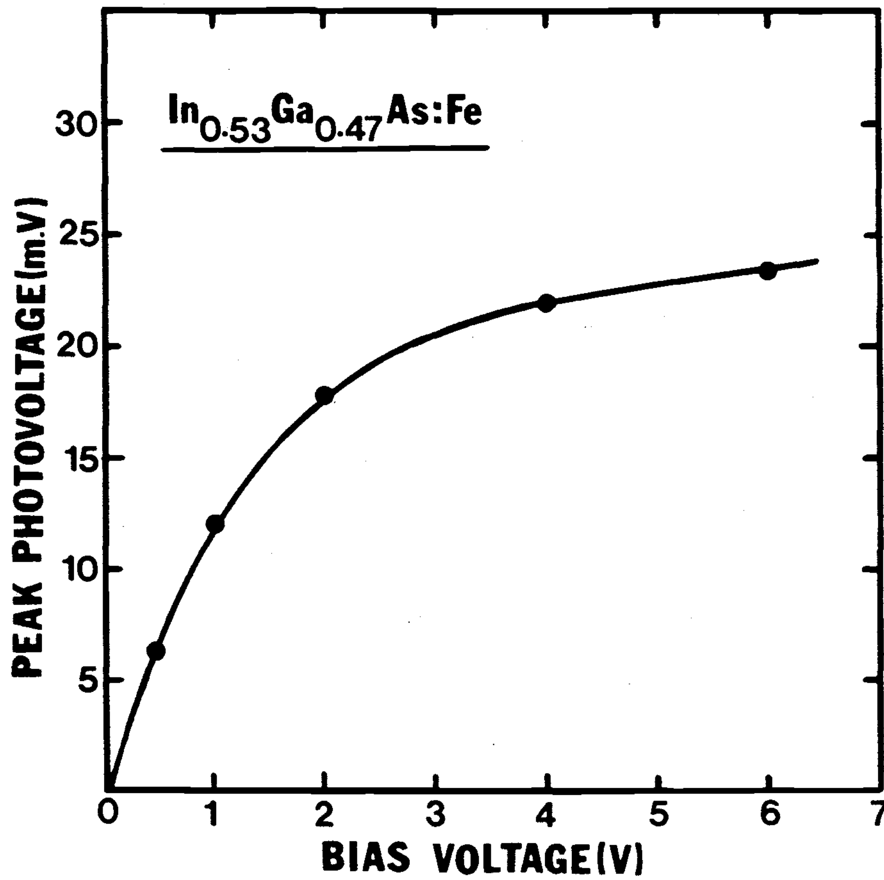

Figure 5.5 Variation of peak photovoltage with bias in $In_{0.53}Ga_{0.47}As:Fe$ photoconductive detector

5.3.3 D.C Optical Gain Measurements

The experiemental setup used for d.c optical gain measurements is shown in Fig. 5.6. The variations of internal optical gain given by Eqn. 4.13 with bias voltage in devices made on Fe-and Zn-doped alloys are shown in Fig. 5.7. Excitation was provided with a 0.63 μm He-Ne laser. The Zn-doped device exhibits higher gain due to higher minority carrier (electron) mobility and possibly higher carrier life time. The measured gains of 8 and 11 in these devices at 6V are amongst the highest values reported. Still higher values can be expected with smaller channel lengths. At very low bias values, the injected electron-hole pair lifetime is determined mainly by bulk and surface recombination so that photoexcited pairs recombine before reaching the contact. With increasing bias, the minority-carrier transit time decreases and the gain increases. The initial linear increase of gain with bias is in accordance with Eqn. 4.14. Values of $\mu_{n,p}$ = 300, 400 ps and $(\mu_n + \mu_p)$ = 6400, 8200 $cm^2/V.s$ for Fe and Zn-doped material, respectively, give reasonable fits to the initial regions of the data. η_i is typically 80-90% in the devices. The subsequent small increase of G_{opt} with bias is probably caused by a combination of carrier velocity saturation and amplification induced by avalanching. The latter may be facilitated by the relatively small bandgap(31).

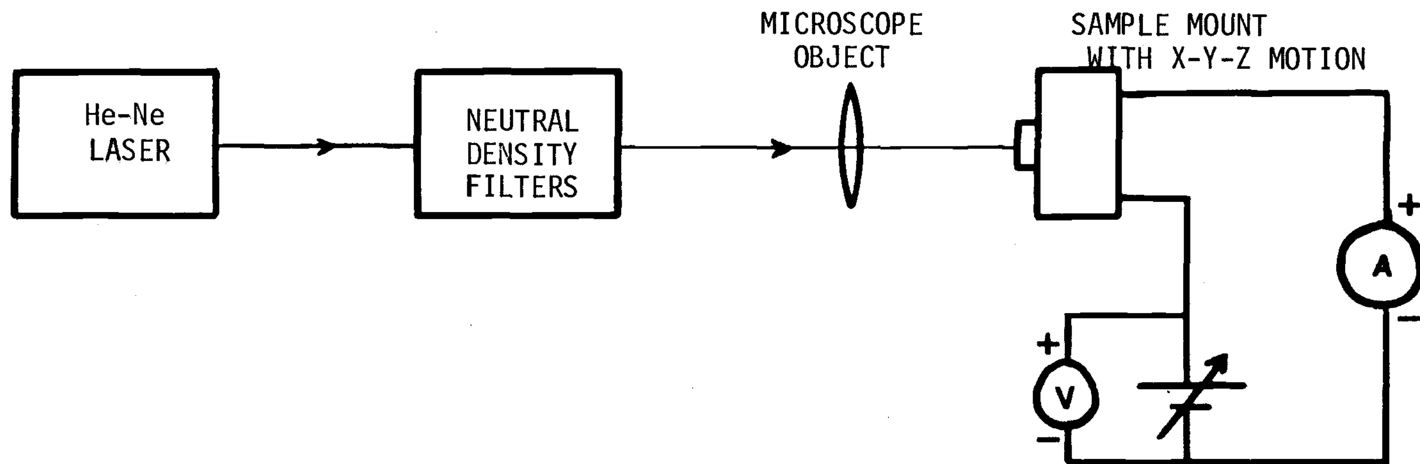

Figure 5.6 Setup for dc optical gain measurements.

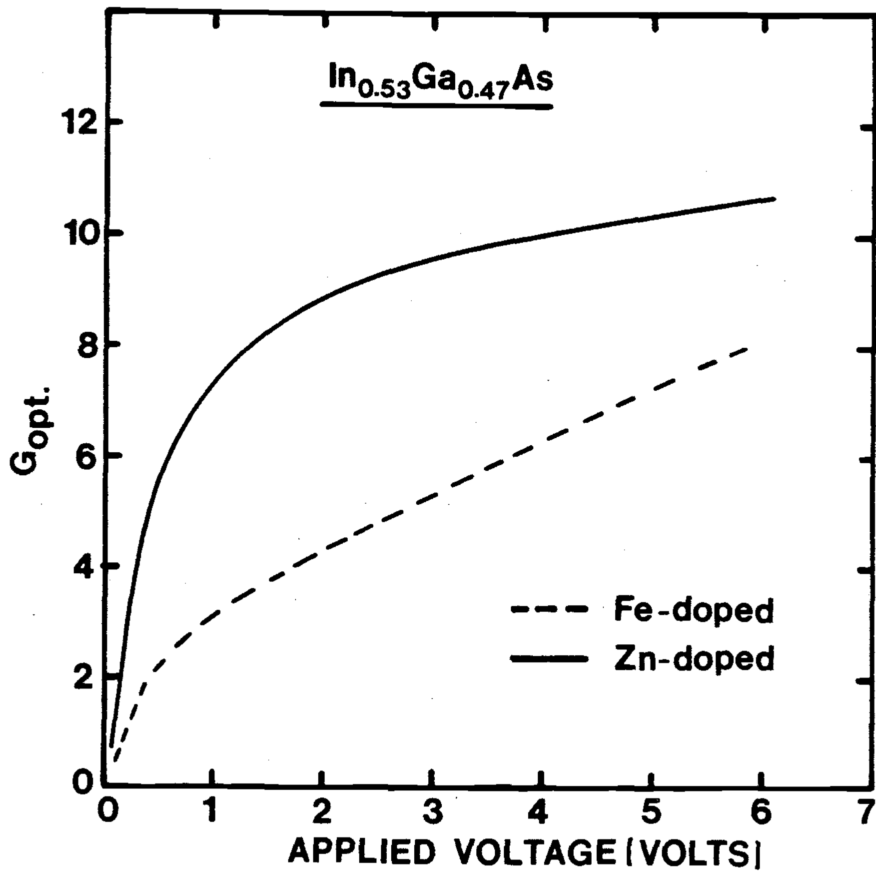

Figure 5.7 Variation of internal optical gain with bias in $In_{0.53}Ga_{0.47}As$:Fe and $In_{0.53}Ga_{0.47}As$:Zn photoconductors.

The sensitivity of Fe and Zn-doped devices are 2.2 and 3.2 A/W, respectively, at a bias of 2V.

An estimate of optical gain can be made from theoretical considerations as follows. In the case of the $In_{0.53}Ga_{0.47}As:Zn$ detector, the applied field is 3kV/cm for a bias of 2V. Assuming the electron drift velocity to be 2×10^7 cm/sec., a value of $t_r \sim$ 35 ps is obtained. An internal optical gain of 11 is then obtained with $\tau_n = 400$ ps, which is a reasonable assumption for the material used in this study. The calculated gain compares favorably with the measured value of 9, as seen in Fig. 7. The internal optical gain is also related to the external quantum efficiency by the relation: $G_{ext} = (1-R)(1-e^{-\alpha d})G_{opt}$. For an applied bias of 2V, the sensitivity of the test diode is 3.15 A/W. G_{ext} is then obtained by knowing the sensitivity of the standard Si-diode. Using reflectivity R = 0.3 and layer thickness d = 5µm, $G_{opt} = 11$ is obtained. Similar calculations lead to values of $G_{opt} = 8$ to 10 at a bias of 2V for the $In_{0.53}Ga_{0.47}As:Fe$ photodetectors, whereas the measured gains are lower. It can only be assumed that non-radiative recombination in the bulk reduces τ and therefore G_{opt}.

The variation of G_{opt} with temperature at different incident power levels is depicted in Fig. 5.8. The measurements were performed with a 0.63 µm He-Ne laser. It is apparent that the variation of carrier mobility and lifetime with temperature is responsible for the observed trend in the gain. The solid lines

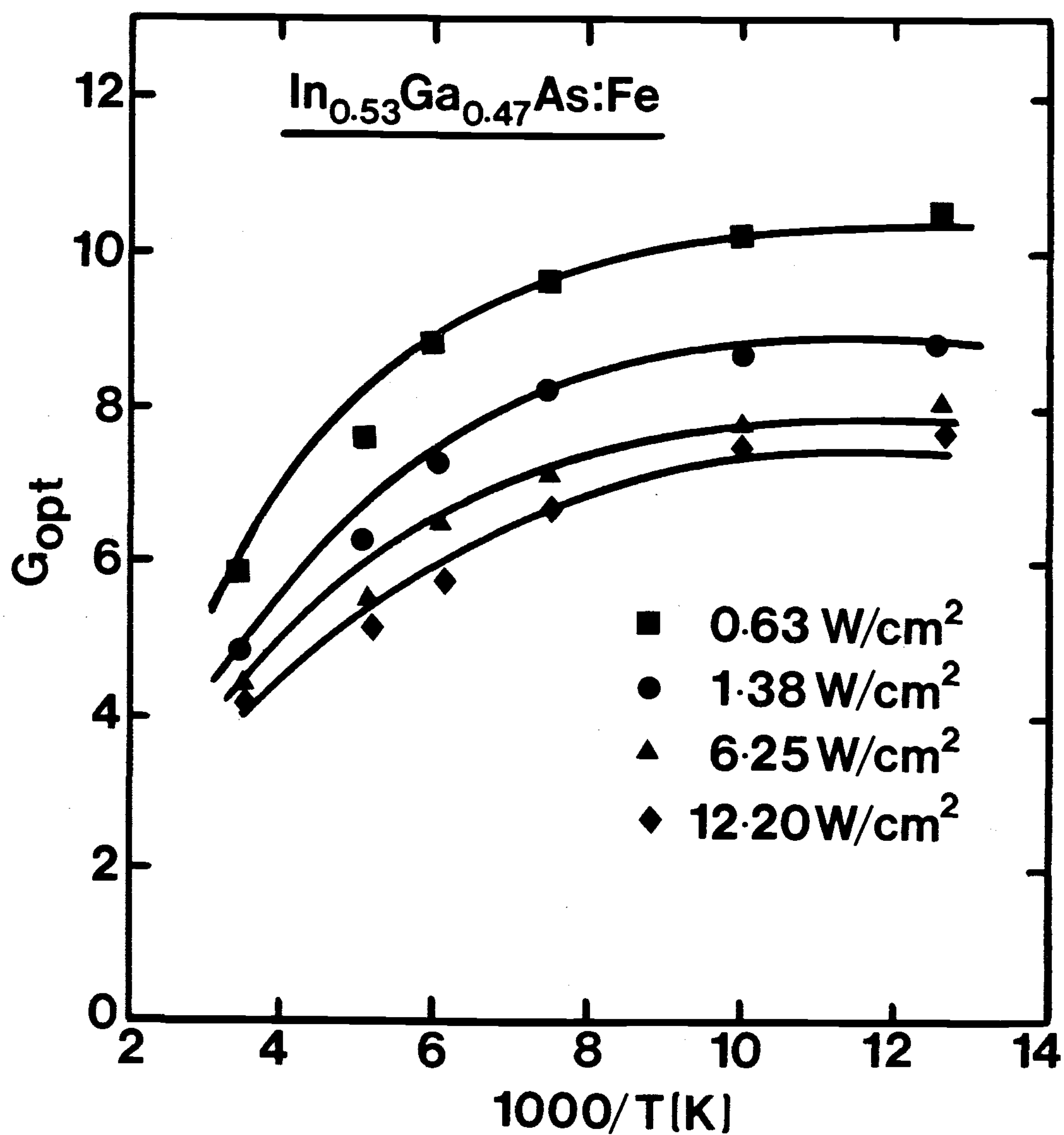

Figure 5.8 Variation of internal optical gain with temperature at various levels of excitation intensity.

in Fig. 5.8 indicate theoretical values of G_{opt} calculated from estimated values of carrier mobility and lifetime. The material parameters used in the analysis are identical to those given in Appendix II. The decrease in gain with increasing light power is due to the decrease in the value of τ_{eff} with increasing light intensity(68). It has been assumed that τ_{eff} varies in the range 300-400 ps with decreasing light intensity under conditions in which the data of Fig. 5.8 were obtained. However, the temperature dependence of τ_{eff} has not been considered. Similar trends are reflected in Fig. 5.9 which depicts the variation of G_{opt} with bias voltage in a Fe-doped device under varying excitation levels.

5.3.4 Noise Characteristics

The conductance of a photoconductor in the dark, G, consists of the conductance due to the dark current and the background current. The thermal noise resulting from G at a temperature T can be expressed as

$$i_G^2 = 4kTGB \qquad (5.1)$$

where k is Boltzmann's constant and B is the bandwidth. The generation-recombination noise induced by the dark current I_d is given by

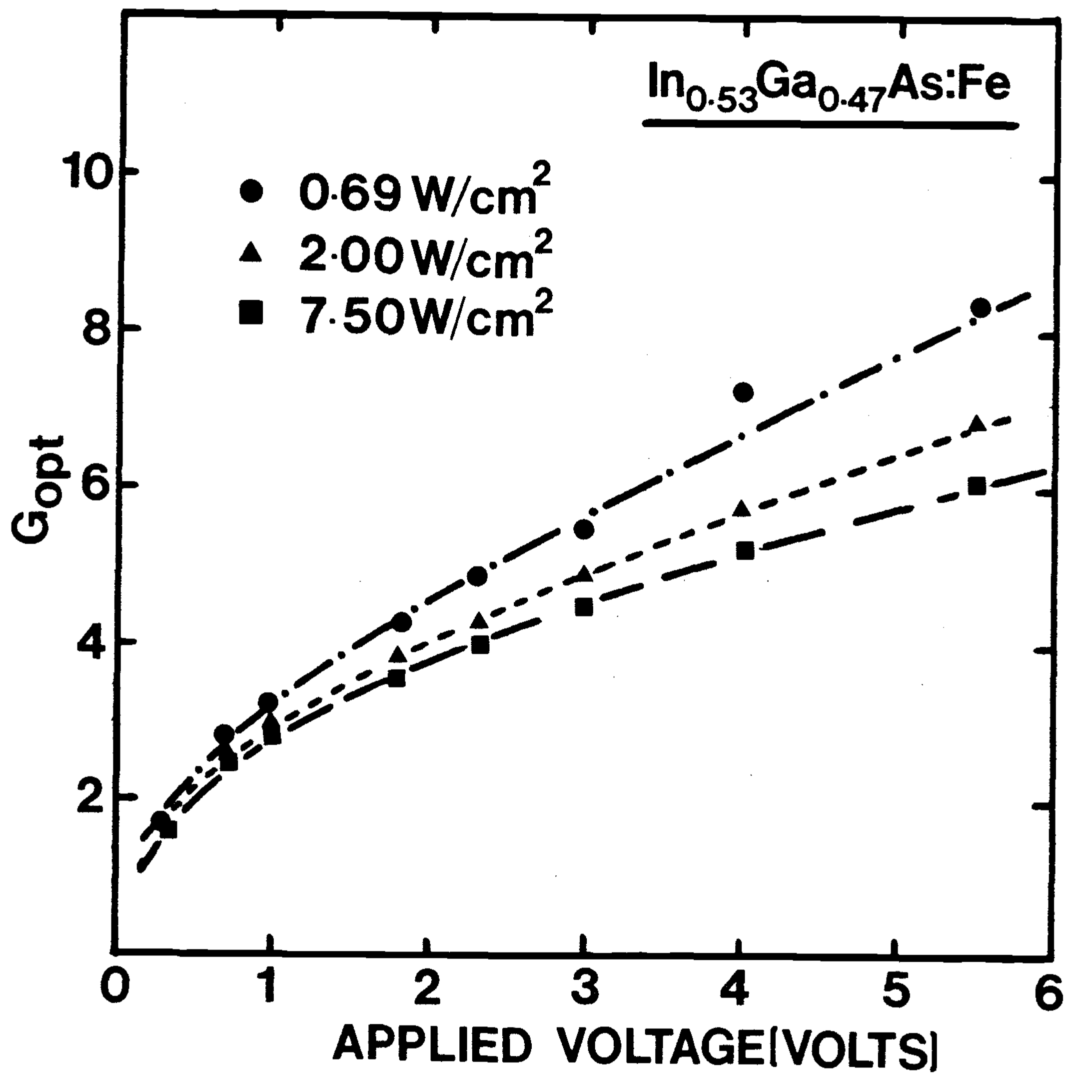

Figure 5.9 Variation of internal optical gain with applied bias at various levels of excitation intensity.

$$i_{GR}^2 = \frac{\tau}{t_r} \frac{4\, q\, I_d\, B}{1 + \omega^2 \tau^2} \qquad (5.2)$$

where ω is the modulation frequency.

Noise measurements on the $In_{0.53}Ga_{0.47}As$:Fe photoconductors were performed in the dark. Under dark conditions, fluctuations in the generation and recombination processes that establish the dark conductance determine the noise power of the device[64]. The experimental setup used for the noise measurements is shown in Fig. 5.10. The background noise level of the whole system at different frequencies is -110 +0.6dBm. The dark currents measured at room temperature in the devices made on Fe-doped $In_{0.53}Ga_{0.47}As$ are so small that the noise measurements almost represent the system limit. Measurements were therefore performed at higher temperatures in the frequency range of 100MHz to 1GHz. The variation of dark current with temperature at a bias of 3.5V is shown in Fig. 5.11 and the frequency dependence of noise power at 1.2MHz noise bandwidth for two dark current levels, 50 and 400 µA, is shown in Fig. 5.12. It should be noted that the data for 50 µA, recorded at room temperature, represents the system limit. It is seen that the noise power at 82°C (400 µA) decreases with increasing frequency in accordance with Eqn. (5.2) and makes the detector very useful for high frequency applications. This behavior is believed to be due to generation-recombination processes [69] in the active channel

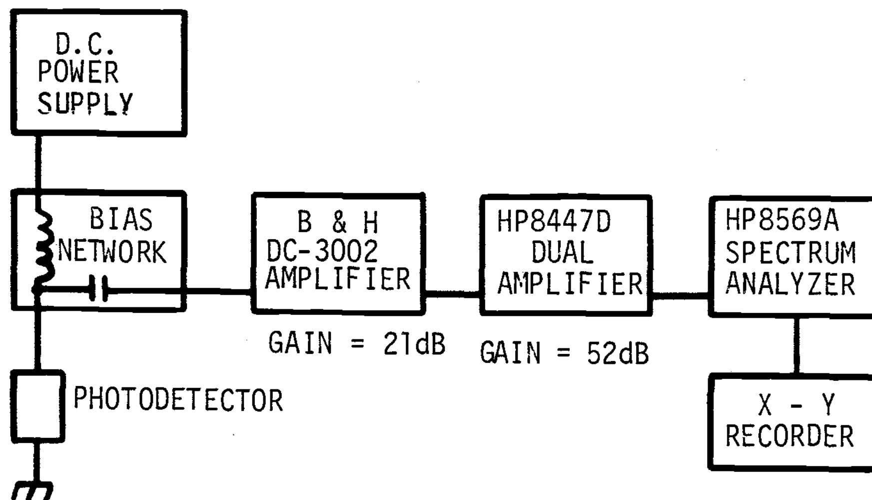

Figure 5.10 Schematic for noise measurements

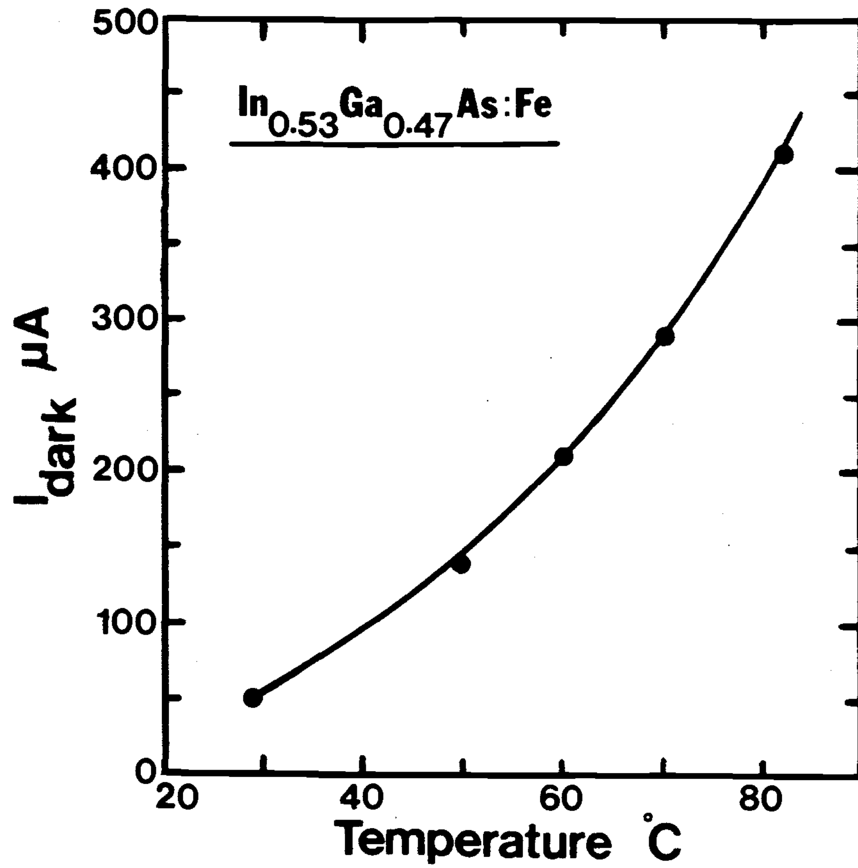

Figure 5.11 Variation of dark current with temperature in $In_{0.53}Ga_{0.47}As$:Fe photoconductive detector.

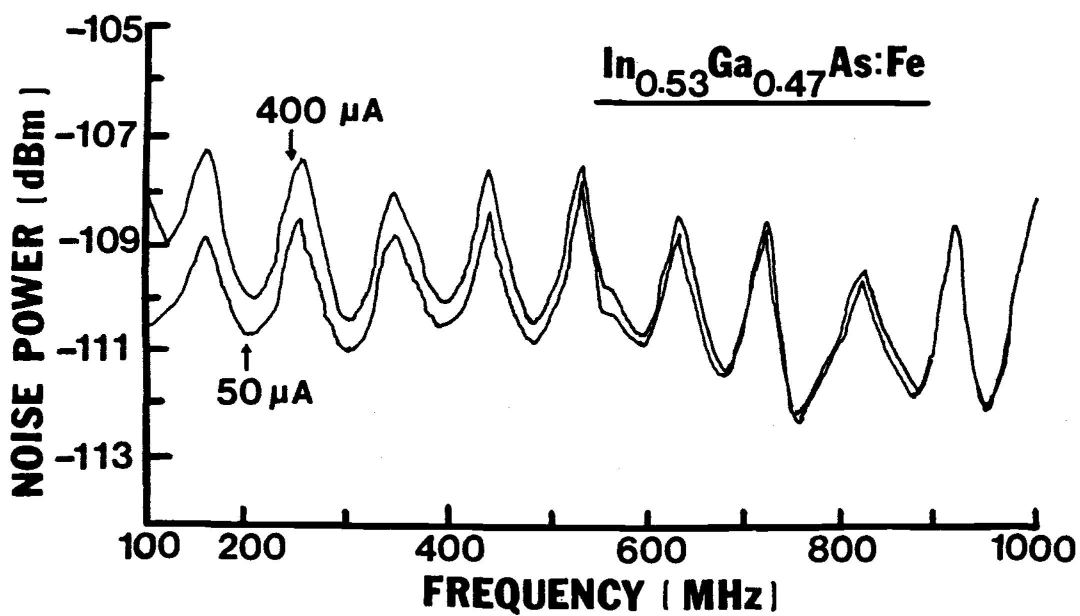

Figure 5.12 Dependence of noise power on frequencies in $In_{0.53}Ga_{0.47}As$:Fe photoconductive detector.

region. The measured noise power at 82°C into a 50 Ω load at 200 MHz and 3.5V bias is -108.9dBm and is one of the lowest values reported till date. The thermal noise power of the resistive channel is given by Eqn. (5.1). Taking B = 1.2MHz and assuming the shunt conductance to be equal to the dc conductance, the calculated noise power is much lower than -110dBm. This suggests that thermal noise is not a contributing factor. By increasing the dark current from 50 μA (28°C) to 400 μA (82°C), the noise power at 200 MHz increased by 1.1dB. This is due to an increase in thermal generation noise. As shown in Fig. 5.12, the effect of temperature on noise power is very small at high frequencies. The dependence of noise power on bias voltage was also studied. The noise power increased with increasing bias voltage due to the increase in dark current and the rate of increase was smaller at higher frequencies. The noise levels observed in the devices are the lowest among the reported values on similar devices.

CHAPTER VI

CONCLUSIONS

High-purity $In_{0.53}Ga_{0.47}As$ has been grown by different melt baking schemes on semi-insulating Fe-doped InP substrates using liquid phase epitaxy. Layers with low background impurity concentrations (N_D, $N_A \sim 10^{14}$ cm^{-3}) and high mobilities μ_{300K} = 10,200 $cm^2/V.s$ and μ_{77K} = 60,000 $cm^2/V.s$) have been grown by long-term baking of melt In, InAs and GaAs. Detailed photoluminescence measurements were made on the layers grown by different melt baking conditions. The strongest peak at the highest energy in the spectra is assigned to bound excitonic transitions. Zn is the main residual background acceptor impurity with $E_A = 28.0 \pm 1.0$ meV. Carbon acceptors with E_A = 13.0 ± 1.0 meV have also been detected occasionally. From variable temperature Hall data a deep level at 0.18 eV below the conduction band has been observed in high purity layers heat-treated at 670°C for 10 min in a flowing H_2 ambient.

It is demonstrated that high resistivity $In_{0.53}Ga_{0.47}As$ can be reproducibly grown at 650°C with the incorporataion of Fe in the growth melt. Epitaxial layers with net electron concentrations as low as 1.5×10^{12} cm^{-3} have been grown. Compensation is produced by a deep level arising from Fe and located 0.46 eV above the valence band. No additional feature is seen in the

4.2K band-edge photoluminescence spectra of Fe-doped $In_{0.53}Ga_{0.47}As$. Chromium doping fails to produce high resistivity material under identical growth conditions. Instead, the net electron concentration increases with increased addition of Cr to the growth melt. It is thought that the Cr itself or a complex defect involving Cr produces a donor level. Transitions at lower energies to the band-to-band transitions by 24.0 meV are observed in the 4.2 K photoluminescence spectra of Cr-doped layers.

Lightly doped p-type $In_{0.53}Ga_{0.47}As$ could be grown with good reproducibility by applying a novel doping technique, where GaAs:Zn is the dopant source. The analysis of variable-temperature hole mobility data of these samples revealed that acoustic deformation-potential and non-polar optical phonon scattering mechanisms play the most dominant role in limiting hole mobility at high temperatures.

From this study, it is seen that Fe-doped $In_{0.53}Ga_{0.47}As$/InP photoconductive detectors can have internal optical gains comparable to devices made with Zn-doped layers. The gains measured in the devices are amongst the highest and the dark currents are the lowest for comparable devices reported in the literature. The external sensitivity of the devices is 3.2 A/W. Optimization of the device paramters will lead to higher values. The response time of the devices is lower than the devices made with n- and p-type layers.

Some suggestions may be made for future work intended to extend the scope of the present study. Further investigations on the behavior of Cr and other transition metal impurities in $In_{0.53}Ga_{0.47}As$ are in order. It is also necessary to investigate further the performance of $In_{0.53}Ga_{0.47}As$:Fe photoconductive detectors by more careful choice of material parameters and optimal device design. It is of great interest to study the monolithic integration of these devices with MISFETs made on the same material.

REFERENCES

1. T.P. Pearsall, IEEE J. Quantum Electron, QE-16, 709 (1980).
2. G.E. Stillman, L.W. Cook, G.E. Bulman, N. Tabatabaie, R. Chin, and P.D. Dapkus, IEEE Trans. Electron. Dev., ED-29, 1355 (1982).
3. M.A. Littlejohn, J.R. Hauser, and T.H. Glisson, Appl. Phys. Lett., 30, 242 (1977).
4. J.D. Oliver and L.F. Eastman, J. Electron. Mater., 9, 693 (1980).
5. S.R. Forrest, R.F. Leheny, R.E. Nahory, and M.A. Pollack, Appl. Phys. Lett., 37, 322 (1980).
6. K. Li, E. Rezek, and H.D. Law, Electron. Lett., 20, 197 (1984).
7. H.H. Wieder, A.R. Clawson, D.I. Elder, and D.A. Collins, IEEE Electron Dev. Lett., EDL-2, 73 (1981).
8. D. Fritzsche, E. Kuphal, and G. Weimann, Proc. Int. Conf. Solid State Devices, Tokyo (1982), Suppl. of Jap. J. Appl. Phys., 22, 591 (1983).
9. E. Kuphal and A. Pocker, J. Crystal Growth, 58, 133 (1982).
10. K.T. Ip, L.F. Eastman and V.L. Wrick, Electron, Lett., 13, 682 (1977).
11. D.E. Holmes and G.S. Kamath, J. Crystal Growth, 54, 51 (1981).
12. S.H. Groves and M.C. Plonko, J. Crystal Growth, 54, 81 (1981).
13. T. Amano, K. Takahei and H. Nagai, Japan. J. Appl. Phys., 20, 2105 (1981).
14. B.L. Mattes, Y. Houng and G.L. Pearson, J. Vac. Sci. Technol., 12, 869 (1975).

15. M. Otsubo and H. Miki, J. Electrochem. Soc., 124, 441 (1977).

16. D.W. Woodard, P.D. Kirchner, W.J. Schaff, S. Tiwari, R. Stall and L.F. Eastman, Inst. Phys. Conf. Ser., 56, 83, (1981).

17. K. Kojima and H. Hasegawa, Phys. Status Solidi (a), 62, 673 (1980).

18. P.A. Houston, J. Electron. Mater., 9, 79 (1980).

19. H. Brendecke, H.L. Stormer and R.J. Nelson, Appl. Phys. Lett., 35, 772 (1979).

20. K. Alavi, R.L. Aggarwal and S.H. Groves, Phys. Rev., B21, 1311 (1980).

21. R.L. Messham, A. Majerfeld and K.J. Bachmann, in Proceedings of the Second International Conference on Semi-Insulating III-V Materials, Editors S. Makram-Ebeid and B. Tuck, (Shiva Publishing Ltd., England, 1982), p. 75.

22. A.R. Clawson, D.P. Mullin and D.J. Elder, J. Cryst. Growth, 64, 90 (1983).

23. T.P. Pearsall, G. Beuchet, J.P. Hirtz, N. Visentin, and M. Bonnet, Proc. Intl. Sympo. GaAs and Related Compounds 1980 (Inst. Phys. Conf. Ser., London), 56, 639 (1981).

24. H. Ohno, C.E.C. Wood, L. Rathbun, D.V. Morgan, G.W. Wicks, and L.F. Eastman, J. Appl. Phys., 52, 4033 (1981).

25. G. Wicks, C.E.C. Wood, H. Ohno, and L.F. Eastman, J. Electron. Mater., 11, 435 (1982).

26. E. Towe, J. Appl. Phys., 53, 5136 (1982).

27. N. Susa, Y. Yamaguchi, H. Ando, and H. Kanbe, J. Crystal Growth, 58, 527 (1982).

28. Y-S. Chen and O.K. Kim, J. Appl. Phys., 52, 7392 (1981).

29. J. Degani, R.F. Leheny, R.E. Nahory, M.A. Pollack, J.P. Heritage, and J.C. Dewinter, Appl. Phys. Lett., 38, 27 (1981).

30. J.C. Gammel, H. Ohno, and J.M. Ballantyne, IEEE J. Quantum Electron., QE-17, 269 (1981).

31. H.J. Klein, R. Kaumanns, and H. Beneking, Electron. Lett., 17, 421 (1981).

32. C.Y. Chen, B.L. Kasper, and H.M. Cox, Appl. Phys. Lett., 44, 1142 (1984).

33. C.Y. Chen, Y.M. Pang, P.A. Garbinski, A.Y. Cho, and K. Alavi, Appl. Phys. Lett., 43, 308 (1983).

34. C.Y. Chen, Y.M. Pang, K. Alavi, A.Y. Cho, and P.A. Garbinski, Appl. Phys. Lett., 44, 99 (1984).

35. C.Y. Chen, Y.M. Pang, A.Y. Cho, K. Alavi, and P.A. Garbinski, J. Vac. Sci. Technol. B, 2, 262 (1984).

36. C.Y. Chen, H.M. Cox, P.A. Garbinski, and S.G. Hummel, Appl. Phys. Lett., 45, 867 (1984).

37. H.H. Wieder, J.L. Veteran, A.R. Clawson and D.P. Mullin, Appl. Phys. Lett., 43, 287 (1983).

38. P.K. Bhattacharya and S. Srinivasa, J. Appl. Phys., 54, 5090 (1983).

39. K. Nakajima, S. Yamazahaki, T. Takanohashi, and K. Akita, J. Crystal Growth, 59, 572 (1982).

40. K. Nakajima, GaInAsP Alloy Semiconductors, Edited by T.P. Pearsall (John Wiley & Sons Ltd., New York, 1982), p. 43.

41. T.P. Pearsall, M. Quillec, and M.A. Pollack, Appl. Phys. Lett., 35, 342 (1979).

42. T.P. Pearsall, R. Bisaro, R. Ansel, and P. Merenda, Appl. Phys. Lett., 32, 497 (1978).

43. V.G. Keramidas, S. Mahajan, H. Temkin, and W.A. Bonner, Inst. Phys. Conf. Ser., 56, 95 (1981).

44. G.H. Olsen, and M. Ettenberg, J. Appl. Phys., 45, 5112 (1974).

45. L.W. Cook, M.M. Tashima, N. Tabatabaie, T.S. Low, and G.E. Stillman, J. Crystal Growth, 56, 475 (1982).

46. Y.P. Varshni, Physica, 39, 149 (1967)

47. P.K. Bhattacharya, M.V. Rao, M.J. Tsai, J. Appl. Phys., 54, 5096 (1983).

48. M.H. Brodsky and G. Lucovsky, Phys. Rev. Lett., 21, 990 (1968).

49. A. Pinczuk, J.M. Worlock, R.E. Nahory, and M.A. Pollack, Appl. Phys. Lett., 33, 461 (1978).

50. J. Shah, R.F. Leheny, R.E. Nahory, and M.A. Pollack, Appl. Phys. Lett., 37, 475 (1980).

51. M.V. Rao and P.K. Bhattacharya, Electron. Lett., 19, 196 (1983).

52. J.K. Rhee and P.K. Bhattacharya, J. Electron. Mater., 11, 979 (1982).

53. K. Kajiyama, Y. Mizushima and S. Sakata, Appl. Phys. Lett., 23, 458 (1973).

54. D.V. Morgan and J. Frey, Electron. Lett., 14, 737 (1978).

55. J.L. Veteran, D.P. Mullin and D.I. Elder, Thin Solid Films, 97, 187 (1982).

56. E. Andre and J.M. LeDuc, Mat. Res. Bull., 4, 149 (1969).

57. E. Kuphal and D. Fritzsche, J. Electron. Mater., 12, 743 (1983).

58. M.M. Tashima, L.W. Cook, G.E. Stillman, Appl. Phys. Lett., 39, 960 (1981).

59. Y. Takeda, M. Kuzuhara, and A. Sasaki, Jap. J. Appl. Phys., 19, 899 (1980).

60. E. Kuphal, J. Cryst. Growth, 54, 117 (1981).

61. A.W. Nelson and P.N. Robson, J. Appl. Phys., 54, 3965 (1983).

62. J.R. Hayes and A.R. Adams, Electron Lett., 16, 282 (1980).

63. H. Beneking, IEEE Trans. Electron Dev., ED-29, 1420 (1982).

64. A. Van der Ziel, Solid State Physical Electronics (Prentice-Hall Inc., New Jersey, 1976), Chap. on 'photoconductivity,' p. 221.

65. C.W. Slayman and L. Figueroa, IEEE Electron Dev. Lett., EDL-2, 112 (1981).

66. R.B. Hammond, N.G. Paulter, R.S. Wagner, T.E. Springer, and M.D.J. MacRoberts, IEEE Trans. Electron Dev., ED-30, 412 (1983).

67. J.C. Gammel, G.M. Metze, and J.M. Ballantyne, IEEE Trans. Electron Dev., ED-28, 841 (1981).

68. A. Rose, in Photoconductivity Conference at Atlantic City, 1954, Editors R.G. Breckenridge, B.R. Russell, and E.E. Hahn (John Wily & Sons, Inc., New York, 1956), p. 3.

69. K.M. van Vliet, Proc. IRE, 46, 1004 (1958).

70. A. Fortini, D. Diguet and J. Lugand, J. Appl. Phys., 41, 3121 (1970).

71. H. Brooks, Advances in Electronics and Electron Physics, Edited by L. Marton (Academic, New York, 1955), p. 156.

72. J.R. Hauser, M.A. Littlejohn, and T.H. Glisson, Appl. Phys. Lett., 28, 458 (1976).

73. L.R. Weisberg, J. Appl. Phys., 33, 1817 (1962).

74. J. Bardeen and W. Shockley, Phys. Rev., 80, 72 (1950).

75. D. Zook, Phys. Rev., 136, A869 (1964).

76. J.D. Wiley, Semiconductors and Semimetals, Vol. 10, Editors R.K. Willardson and A.C. Beer (Academic, New York, 1975), p. 91.

APPENDICES

APPENDIX I

The equations describing the temperature dependence of electron mobility limited by different scattering mechanisms in a ternary semiconductor are outlined below.

I.1 Polar Optical Phonon Scattering

Following the analysis of Fortini et al.[70], the temperature dependence of the electron mobility due to polar optical phonon scattering is given by:

$$\mu_{PO} = 25.44 \frac{\varepsilon_s - \varepsilon_d}{\varepsilon_s - \varepsilon_d} \cdot \frac{\mathrm{Exp}\,(\theta/T) - 1}{(m^*/m_o)^{3/2} T^{-1/2} \cdot \theta} \cdot G\,(\theta/T)\ (\mathrm{cm}^2/\mathrm{V.s}) \qquad (\mathrm{I.1})$$

where θ is the optical phonon temperature, and $G(\theta/T)$ is a function whose temperature variation is given by Fortini et al.[70]

I.2 Ionized Impurity Scattering

The scattering of electrons by singly ionized impurities is described by the Brooks-Herring equation[71]. The temperature dependence of the ionized impurity scattering limited mobility is given by

$$\mu_{II} = \frac{3.28 \times 10^{15} (m_o/m^*)^{1/2} \varepsilon_s^2 T^{3/2}}{(2N_A + n_o) [\ln(b+1) - [b/(b+1)]]} \quad (cm^2/V.s) \qquad (I.2)$$

$$\text{where } b = \frac{1.29 \times 10^{14} (m^*/m_o) \varepsilon_s T^2}{n^*} \qquad (I.3)$$

$$\text{and } n^* = \frac{n_o + (n_o + N_A) (N_D - N_A - n_o)}{N_D} \quad (cm^{-3}) \qquad (I.4)$$

where N_D and N_A are the density of donors and acceptors, respectively. $n^* = n_o \simeq N_D - N_A$ when the donors and acceptors are fully ionized.

I.3 Alloy Scattering

An additional scattering mechanism is present in ternary and quaternary semiconductors due to the random distribution of the component atoms among the available lattice sites. The temperature dependence of the mobility limited by alloy scattering is given by[72]

$$\mu_{AL} = \frac{9.43 \times 10^3}{(m^*/m_o)^{5/2} (\Delta U)^2 a^3 T^{1/2}} \quad (cm^2/V.s) \qquad (I.5)$$

I.4 Space Charge Scattering

From Weisberg's[73] analysis, the space charge scattering limited mobility is given by

$$\mu_{SC} = \frac{(3.2 \times 10^{9})\ T^{-1/2}}{(m^*/m_o)^{1/2}\ (N_s A)} \quad (cm^2/V.s) \qquad (I.6)$$

where N_s is the concentration of space charge and A is the effective scattering area of the space charge region.

I.5 Deformation Potential Scattering

Bardeen and Shockley[74] have derived the mobility limited by this mechanism. The temperature dependence can be expressed as:

$$\mu_{DP} = \frac{(3.2 \times 10^{-5})\ \rho_d v_1^{2}\ T^{-3/2}}{(m^*/m_o)^{5/2}\ E_1^2} \quad (cm^2/V.s) \qquad (I.7)$$

where ρ_d and v_1 are the mass density and the longitudinal sound velocity respectively. E_1 is the deformation potential in electron volts.

I.6 Piezoelectric Scattering

The electron mobility limited by piezoelectric scattering is given by[75]

$$\mu_{PE} = \frac{2.52 \times 10^{12}\ T^{-1/2}}{(m^*/m_o)^{3/2}\ (e_{14}/\varepsilon_s\varepsilon_o)^2\ (4/C_t + 3/C_l)}\ (cm^2/V.s) \qquad (I.8)$$

where $C_l = 1/5\ (3C_{11} + 2C_{12} + 4C_{44})$ (I.9)

$$C_t = 1/5\ (C_{11} - C_{12} + 3C_{44}) \qquad (I.10)$$

are the spherically averaged longitudinal and transverse elastic constants and e_{14} is the piezoelectric constant.

APPENDIX II

MATERIAL PARAMETERS USED FOR ANALYSIS OF $In_{0.53}Ga_{0.47}As$ ELECTRON MOBILITY DATA

Parameter	Symbol	Value
Electron Effective Mass Ratio	m_e^*/m_o	0.034
Alloy Scattering Potential for Electrons	ΔU	0.75
Optical Phonon Temperature	$\theta(K)$	382.9
Piezoelectric Constant	$e_{14}(C/m^2)$	0.099
Low-Frequency Dielectric Constant	ε_S	13.73
High-Frequency Dielectric Constant	ε_d	11.36
Density	$\rho_d(g/cm^3)$	5.55
Sound Speed	v_1 (m/sec)	4.73×10^5
Acoustic Deformation Potential	E_1 (eV)	6.64
Elastic Constant	C_{11} (dyne/cm^2)	1.02×10^{12}
Elastic Constant	C_{12} (dyne/cm^2)	0.51×10^{12}

Elastic Constant	C_{44} (dyne/cm^2)	0.49×10^{12}
Atomic Radius	a(A°)	5.86875
Product of Concentration and Area of Scattering Centers	$N_S \times A$(cm^{-1})	$(0.2\text{-}1.0) \times 10^5$

APPENDIX III

The equations describing the temperature dependence of hole mobility limited by different scattering mechanisms in a ternary semiconductor are described below. Analysis of the hole mobilty data is more complex than that of electrons. For hole mobility, three factors, in addition to those of electrons, must be taken into account.

First, because the light and heavy hole bands are degenerate at the valence band maximum, both types of carrier must be taken into account. Owing to the strong light-hole-band to heavy-hole-band scattering, light holes do not have such a large effect on the transport as would otherwise be expected and, following Wiley[76], they can be taken into account in each scattering mechanism by multiplying equations (I.1), (I.2), (I.5) and (I.6) to an appropriate function of r, where $r = m_h^*/m_l^*$ the ratio of the effective masses of heavy and light holes. Additionally, the surfaces of constant energy for holes are not spherical as for electrons, but have strong p-like symmetry. Taking these factors into account, the equations for the mobility limits imposed by polar optical phonon scattering μ_{PO}^{P}, ionized-impurity scattering μ_{II}^{P}, alloy scattering μ_{AL}^{P}, and space-charge scattering μ_{SC}^{P} then become

$$\mu_{PO}^{P} = 2\ K\ \mu_{PO} \qquad \text{(III.1)}$$

$$\mu^{p}_{ll} = 1.5 \; \frac{1.5\,(r^{1/2} + ra^{3/2})}{(1 + r^{3/2})} \; \mu_{ll} \qquad \text{(III.2)}$$

$$\mu^{p}_{SC} = \frac{r^{5/2}\,(1+ r^{1/2})}{(1 + r^{3/2})^2} \; \mu_{SC} \qquad \text{(III.3)}$$

$$\mu^{p}_{AL} = \frac{r^{5/2}\,(1+ r^{1/2})}{(1 + r^{3/2})^2} \; \mu_{AL} \qquad \text{(III.4)}$$

where μ_{PO}, μ_{ll}, μ_{SC}, and μ_{AL} are obtained from equations (I.1), (I.2), (I.6) and (I.5), respectively using the heavy hole mass m^*_h.

The factor 2 in equation (III.1) and the factor 1.5 in equation (III.2) take into account the p-like symmetry of the hole wavefunctions, and K is a correction factor to take into account the contribution from light holes and is given graphically by Wiley[76]. Finally, when considering hole mobilities, acoustic deformation-potential scattering and also non-polar optical phonon scattering may be combined to give a mobility limit.

$$\mu_{AC+NPO} = 3.17 \times 10^{-4} \; \frac{r^{5/2}\,(1 + r^{1/2})}{(1 + r^{3/2})^2} \; \frac{\rho_d W_l^{\,2}}{(m^*_h/m_o)^{5/2}} \; \frac{S(\theta,\eta,T)}{E^2_{AC}} T^{3/2} \qquad \text{(III.5)}$$

where ρ_d, W_1, and E_{AC} are the density, average sound velocity, and hole deformation potential, respectively, $\eta = (E_{NPO}/E_{AC})^2$ where E_{NPO} is the optical phonon deformation potential and S is a function given graphically by Wiley.

APPENDIX IV

MATERIAL PARAMETERS USED FOR ANALYSIS OF $In_{0.53}Ga_{0.47}As$ HOLE MOBILITY DATA

Parameter	Symbol	Value
Heavy Hole Effective Mass Ratio	$\frac{m_h^*}{m_o}$	0.609
Light Hole Effective Mass Ratio	$\frac{m_l^*}{m_o}$	0.049
Hole Deformation Potential	E_{AC} (eV)	3.341
Optical Phonon Deformation Potential	E_{NPO} (eV)	6.076
Alloy Scattering Potential for Holes	ΔU_p (eV)	0.1